Figure 9.22. Monte Carlo electron-trajectory calculations of the normalized intensity (I_{diam}/I_{bulk}) as a function of diameter for spherical particles of NIST glass K-309(15% Al_2O_3, 40% SiO_2, 15% CaO, 15% Fe_2O_3, 15% BaO).

Figure 9.23. Monte Carlo electron-trajectory calculation of the emission of x-rays from a tilted specimen of iron, with the intensity normalized to 0° tilt. Beam energy = 20 keV.

Figure 9.24. Schematic diagram comparing the absorption path in a particle with the equivalent path in a bulk target.

Absorption Path in Solid

Path in Particle

Figure 9.25. Schematic diagram showing the dramatic differences in the absorption path when the beam is located on the front face (toward the detector, 1), on the top (2), and on the back face (3) of the particle.

Extra Absorption Path From Position 3

Figure 9.26. Energy-dispersive x-ray spectra obtained from a 20-μm-diameter spherical particle of NIST SRM glass K-411 (15% MgO, 55% SiO₂, 15% CaO, 15% FeO). The gold peak is an artifact from the sputtered coating. (a), (c) Front face, toward the detector. (b), (d) Back face, away from the detector. (e) Comparison of the overlaid spectra normalized at Fe $K\alpha$ showing large attenuation of the low-energy portion below 5 keV.

Figure 10.1. X-ray dot map (area scan) of a ternary alloy: (a) Specimen-current (inverted contrast) image showing atomic number contrast; (b) Dot map of silver ($L\alpha$); (c) Dot map of copper ($K\alpha$); (d) Dot map of tin ($L\alpha$). The dot maps have been prepared with the characteristic x-ray signal derived from a wavelength-dispersive x-ray spectrometer. (Courtesy of Robert Myklebust, NIST.)

present in the unknown at a level of 10 wt %, the count rate is reduced
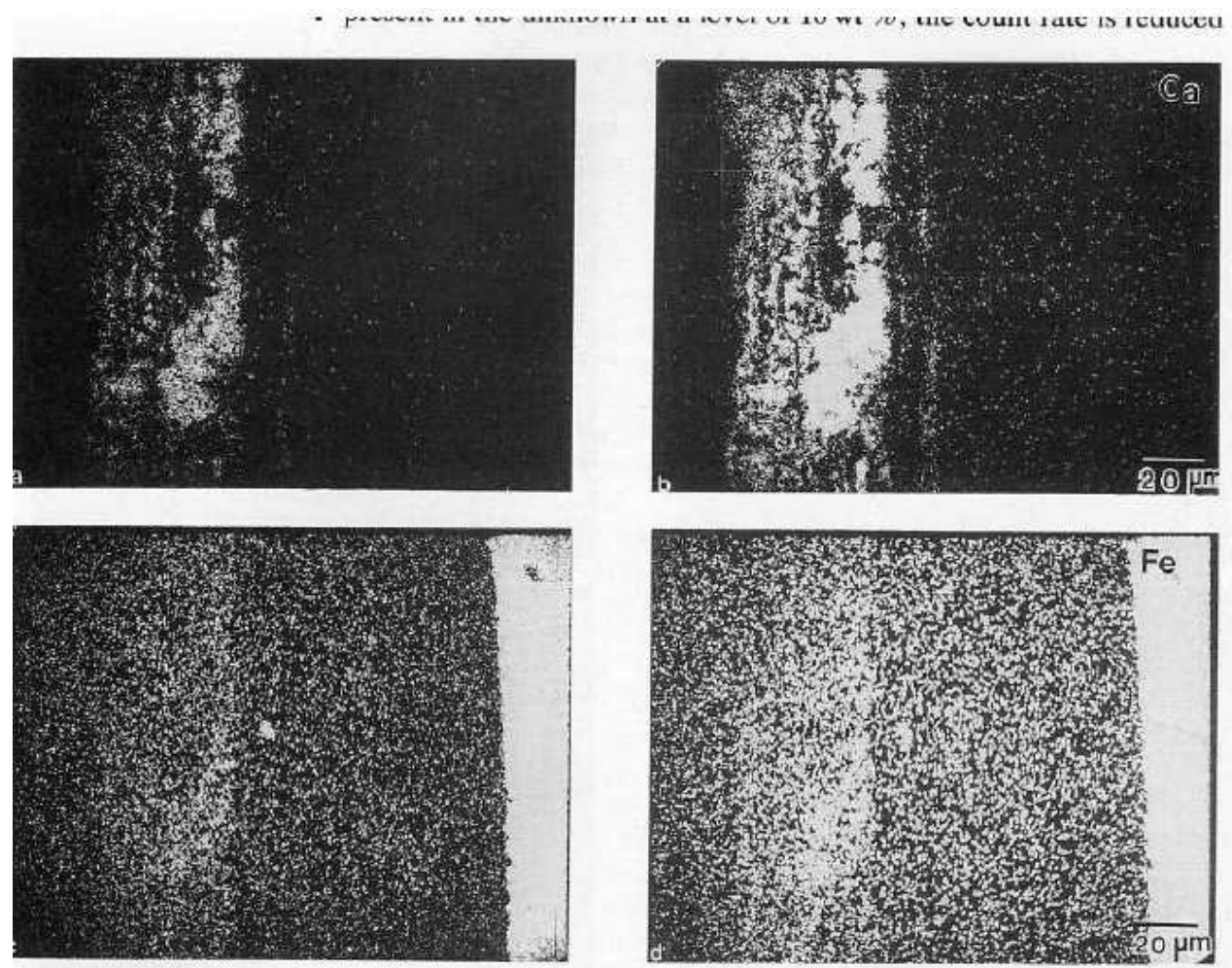
Figure 10.2. Choice of recording parameters in x-ray dot mapping. Effects of number of dots: (a) Good contrast found in high-concentration region with 10,000 dots recorded; (b) further accumulation to 40,000 dots leads to improved contrast in lower-concentration area at the expense of saturation in higher-concentration region. Choice of dot brightness: (c) Properly adjusted CRT dot; (d) dot adjusted to be too bright (note loss of contrast in image.) Specimen: coating on steel; $E_0 = 20$ keV. (a) and (b) Ca $K\alpha$; (c) and (d) Fe $K\alpha$. (Courtesy of Ryna Marinenko, NIST.)
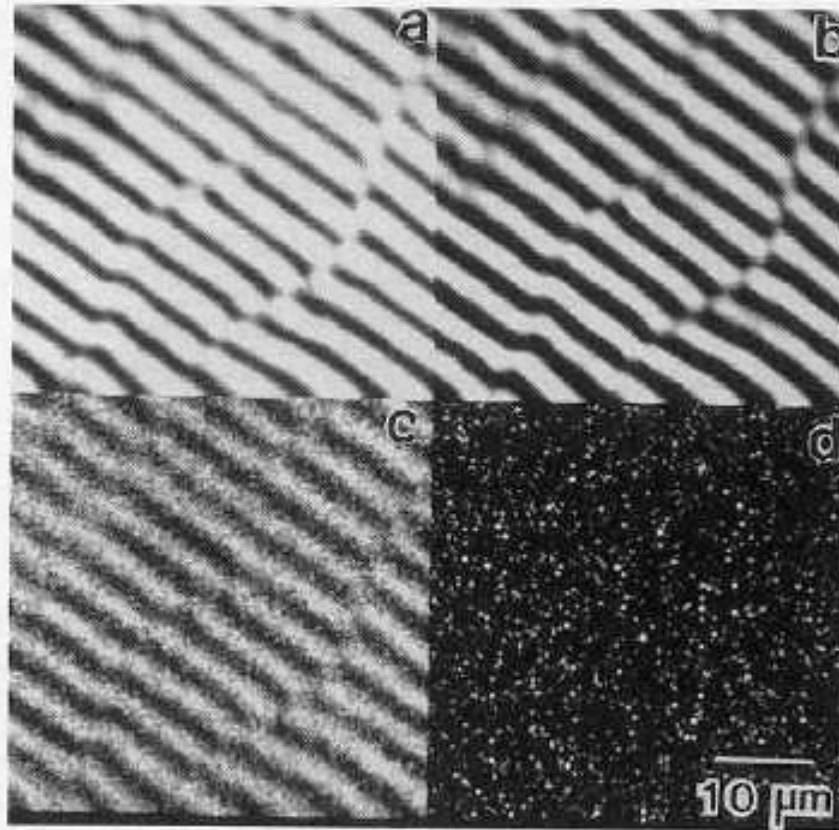
Figure 10.6. Example of false compositional contrast, a mapping artifact which occurs because of the dependence of the x-ray bremstrahhlung on the composition of the specimen. The specimen is aluminum–copper (eutectic). A map has been prepared with the energy-dispersive x-ray spectrometer, with an energy window at the position of (a) aluminum, (b) copper, and (c) scandium. The contrast in image (c) suggests that scandium is present and is preferentially segregated in the copper-rich phase. But no scandium is present. (d) When a proper background correction is applied, the apparent scandium contrast is eliminated (Myklebust et al., 1989).
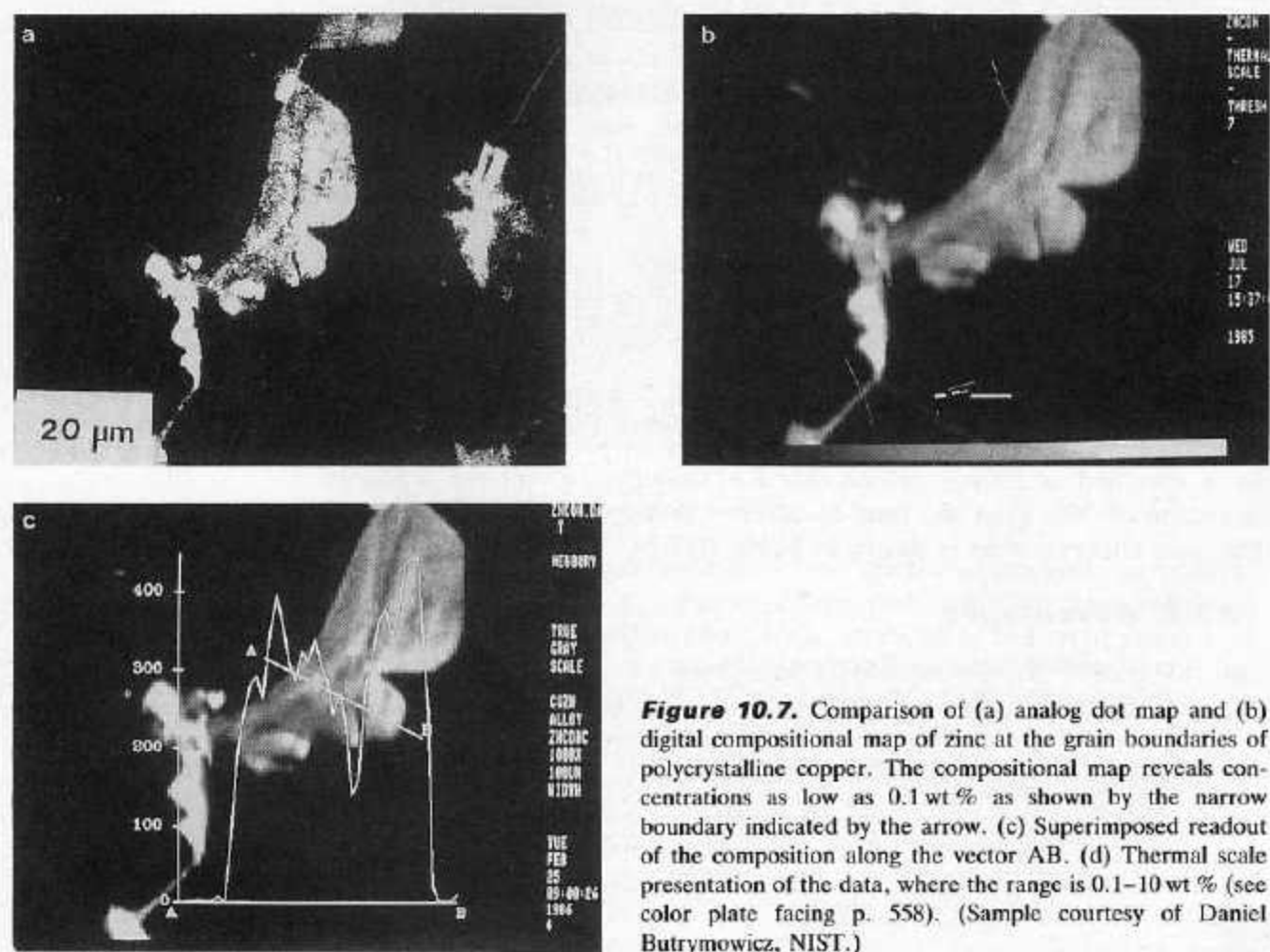
Figure 10.7. Comparison of (a) analog dot map and (b) digital compositional map of zinc at the grain boundaries of polycrystalline copper. The compositional map reveals concentrations as low as 0.1 wt % as shown by the narrow boundary indicated by the arrow. (c) Superimposed readout of the composition along the vector AB. (d) Thermal scale presentation of the data, where the range is 0.1–10 wt % (see color plate facing p. 558). (Sample courtesy of Daniel Butrymowicz, NIST.)

Figure 10.8. Trace-level imaging of trace constituents in human brain tissue: (a) Calcium, white = 7000 parts per million, (b) Aluminum, white = 500 parts per million (Garruto *et al.*, 1984).

Figure 10.9. Compositional maps of a gold–platinum diffusion couple, illustrating the application of image-processing functions: (a) Au map; (b) Pt map, linear gray scale depiction; (c) Au × Pt; (d) Au/Pt; (e) Au and (f) Pt, magnitude of image gradient; (g) Au and (h) Pt, direction of image gradient. (Sample courtesy of C. Handwerker, NIST. Images courtesy of R. Marinenko, D. Bright, NIST.)
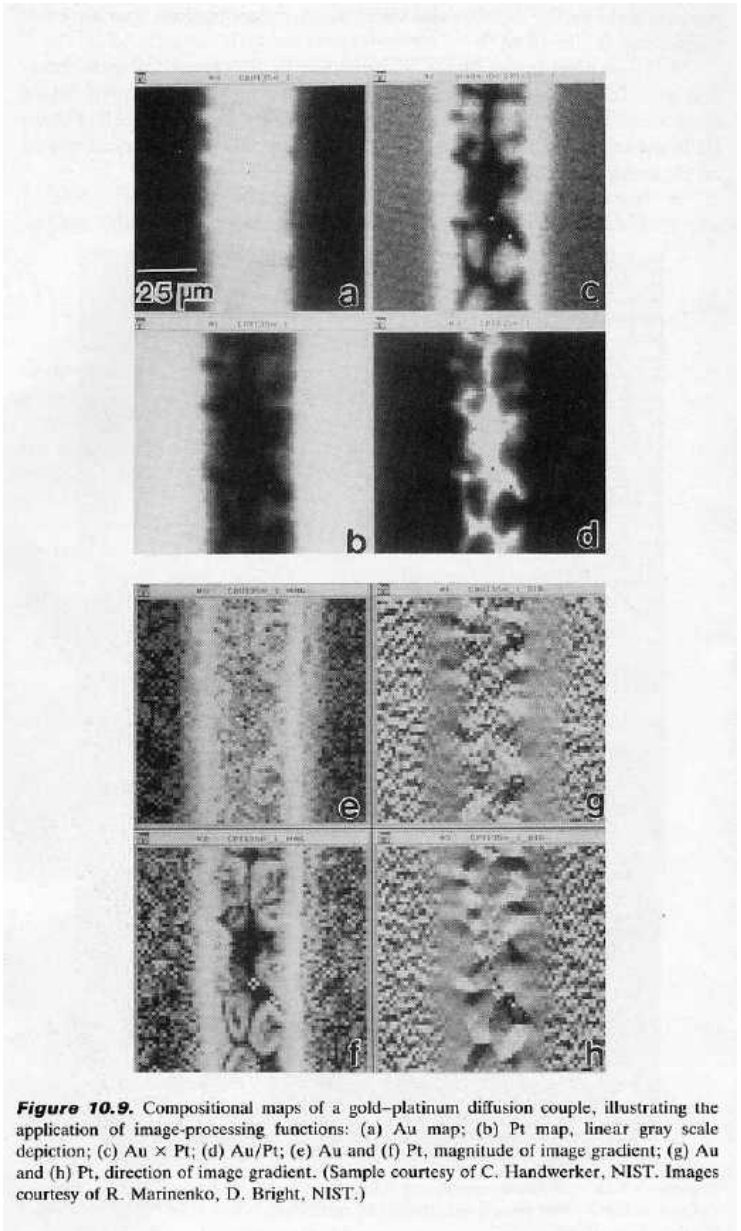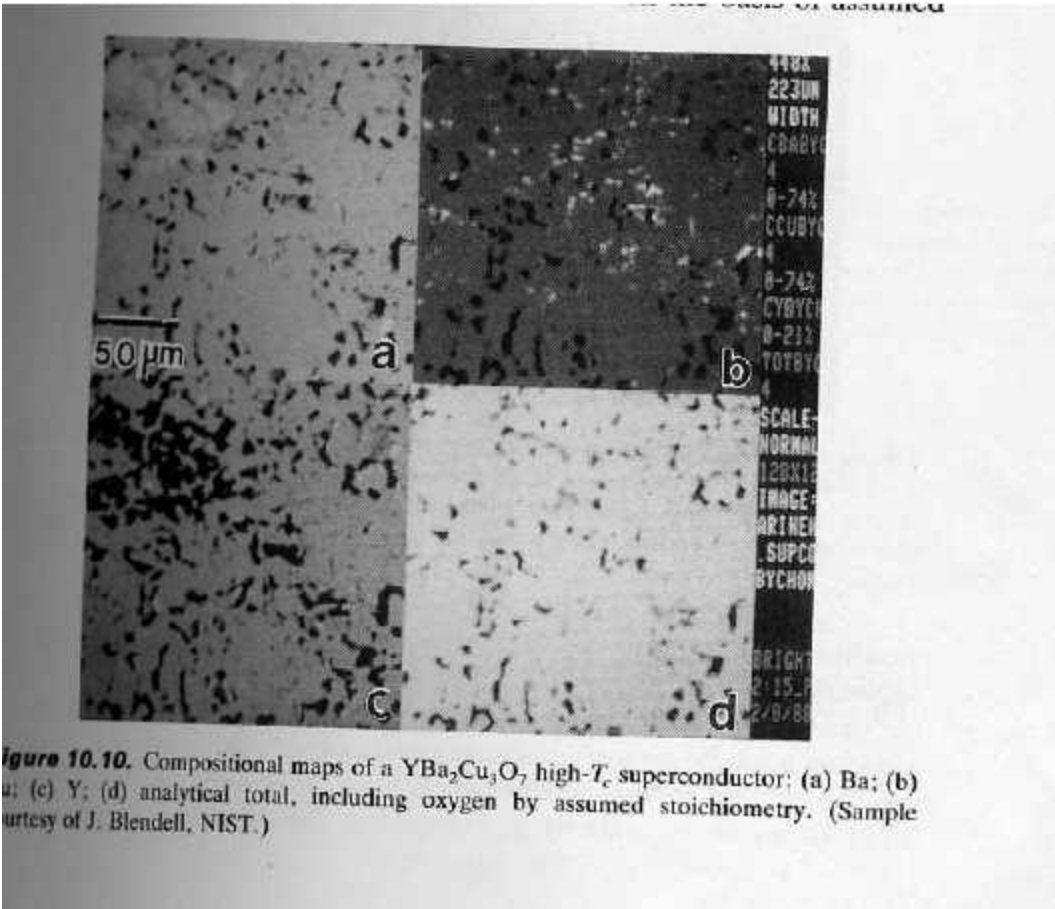
Figure 10.10. Compositional maps of a $YBa_2Cu_3O_7$ high-T_c superconductor: (a) Ba; (b) u; (c) Y; (d) analytical total, including oxygen by assumed stoichiometry. (Sample urtesy of J. Blendell, NIST.)
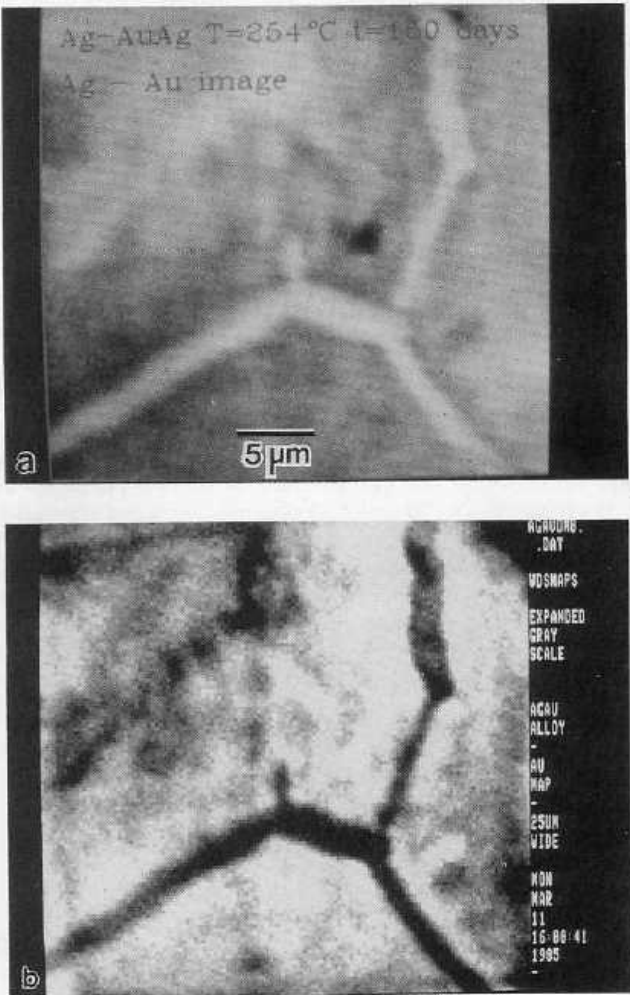
Figure 10.11. Enhancement of compositional contrast at high concentrations. Increase in the silver concentration at grain boundaries of a silver–gold alloy: (a) Compositional map of silver; the bright area represents a 5% increase in silver against a general background of 65% silver; (b) The corresponding gold image, showing a deficit in concentration. (Sample courtesy of Daniel Butrymowicz, NIST.)
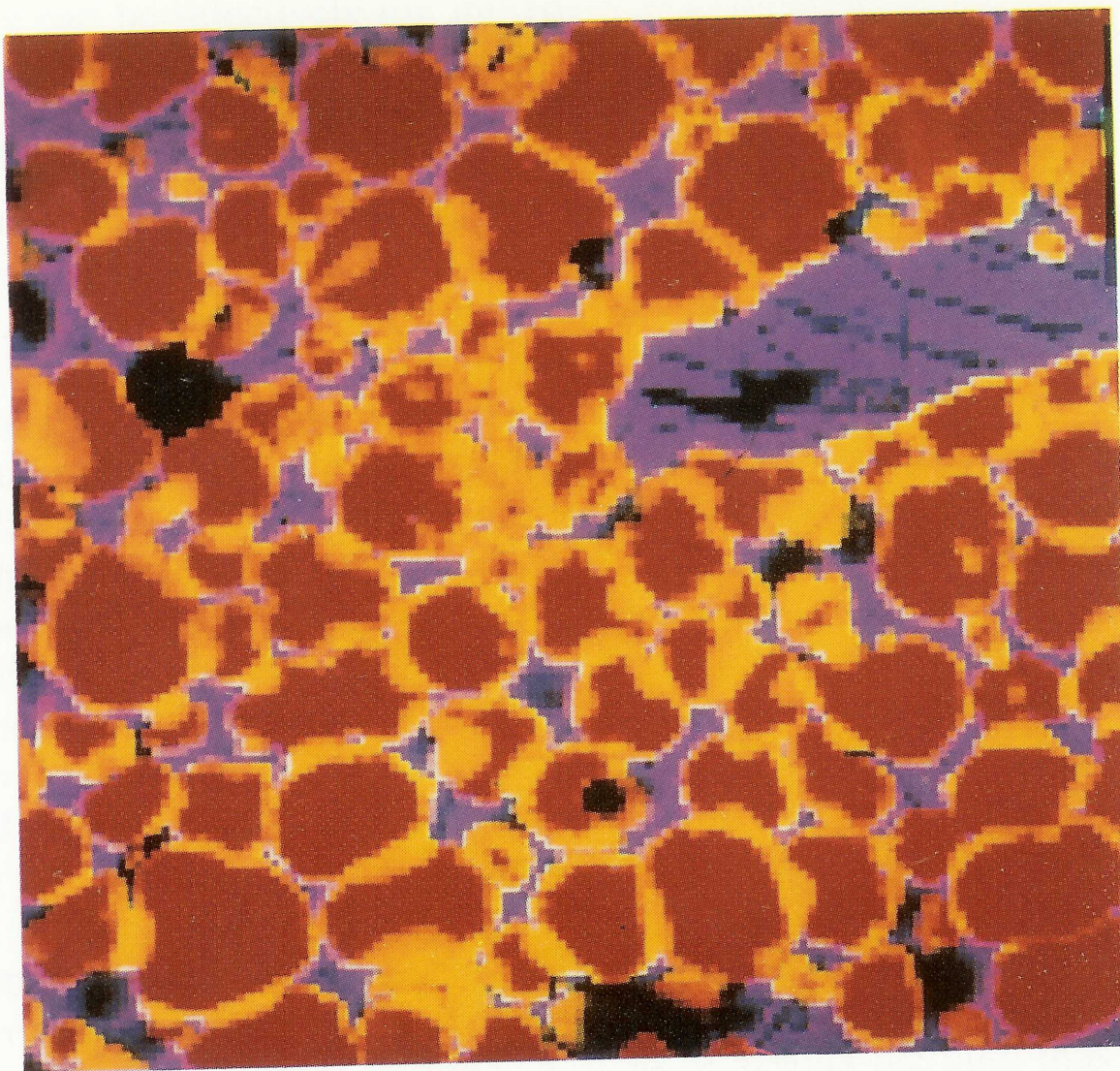
Figure 10.12d. Primary color overlay of compositional maps for a polyphase ceramic: red, magnesium; green, cobalt; blue, vanadium. Note: yellow phase = magnesium + cobalt; purple phase = magnesium + vanadium.

EDS DETECTOR

❖ Li – drifted p-type S1 crystal to produce a wide intrinsic region

❖ Absorption of x-rays finally leads to a number, n, of electrons & holes,
  n= Ex-ray/3.8
  (e.g.,) Cu-Kα, Ex-ray ~ 8000 eV
  n ≈ 2100

❖ Charges are collected & converted to a voltage pulse, V & counted V α E x-ray

❖ Time between counting one x-ray & another ~ 10μsec, i.e.,
  No. of x-rays/sec ≤ 10^5

❖ *TO MINIMISE THERMAL CARRIERS, COOL TO 77 K*

QUALITATIVE ANALYSIS

❖ Automatic peak dentification programmes…….But :

➢ Overlapping peaks from different groups (K, L, M…) of different elements

➢ Sum peaks $[E = E_{k_\alpha} + E_{k_\beta}]$

➢ Escape peaks

➢ Too Low accelerating voltage to excite a peak

➢ Ensure that _ALL_ expected peaks of an element are present _AND_ in the right proportion

- If energy of x-ray is NOT fully utilised in electron-hole pairs additional artefacts occur:

------ Actually measured

--- True profile

① INCOMPLETE COLLECTION OF CHARGES !!

CONTINUOUS X-RAYS GENERATED IN Si ESCAPE WITHOUT COLLECTION
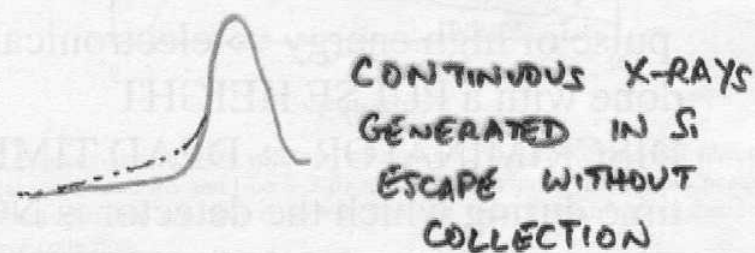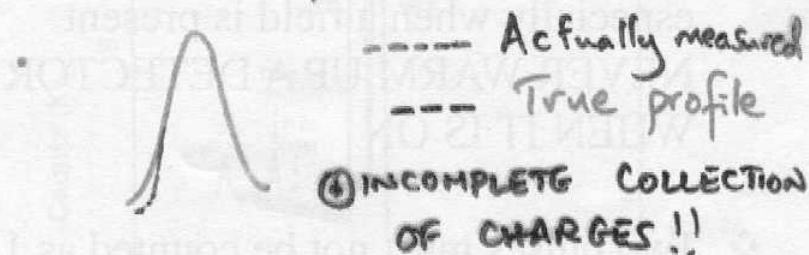
PEAK ↓   BACKGROUND ↑

- ESCAPE PEAKS

$Si - K_\alpha$ x-ray escapes !

Detector counts an energy

$E - E_{Si-K_\alpha}$ = low energy "peak"

PRECAUTIONS IN EDS

❖ Lithium is mobile even at R. T & especially when a field is present NEVER WARM UP A DETECTOR WHEN IT IS ON

❖ Two pulses must not be counted as 1 pulse of high energy $\Rightarrow$ electronically done with a PULSE HEIGHT DISCRIMINATOR $\Rightarrow$ DEAD TIME, i.e., time during which the detector is NOT counting x-rays. IN QUANTITATIVE ANALYSIS COMPARE SPECTRA TAKEN WITH THE SAME "LIVE TIME" = TRUE TIME – DEAD TIME

❖ All peaks have a width which is ~ 100 – 150 eV $\Rightarrow$ variations in 'n' & due to electronic noise
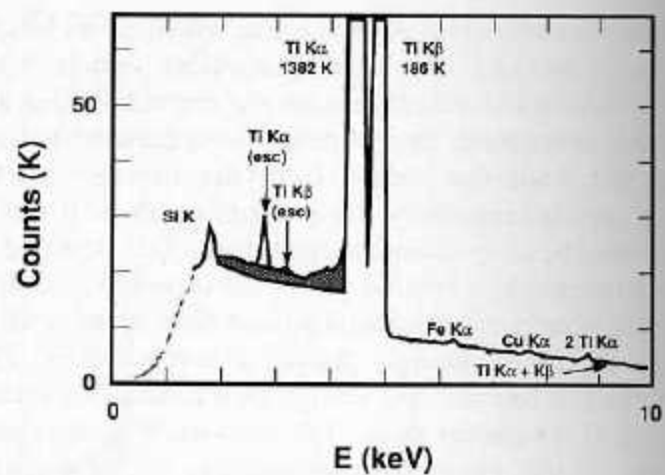
Figure 5.39. Electron-excited EDS spectrum of titanium. The Ti $K\alpha$ and $K\beta$ silicon x-ray escape peaks and the 2 $K\alpha$ and ($K\alpha + K\beta$) sum peaks are noted. Extraneous peaks from the specimen chamber are also observed. Hatched area is contribution due to incomplete charge collection.

Figure 5.53. Schematic drawing of the relationship between the measured and generated spectral distributions of manganese. (Courtesy of R. Bolon.)
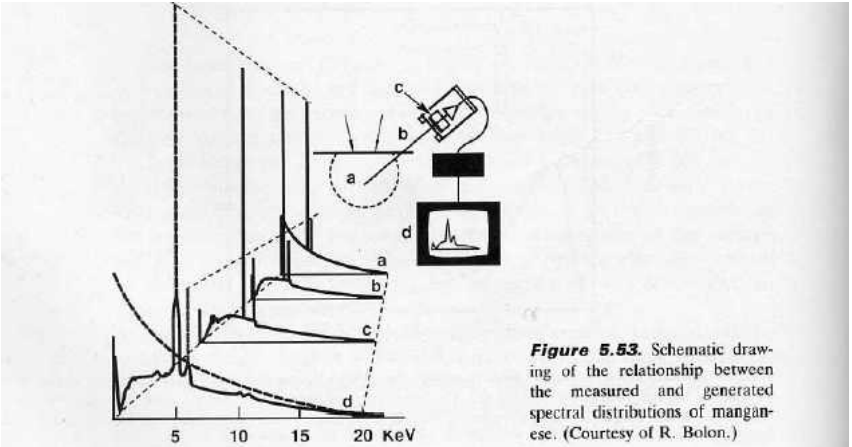
Table 3.14. Secondary Fluorescence in a Sample Containing Mn, Fe, Co, and Ni

Element	Radiation causing fluorescence
Mn	Fe $K\beta$, Co $K\alpha$, Co $K\beta$, Ni $K\alpha$, Ni $K\beta$
Fe	Co $K\beta$, Ni $K\alpha$, Ni $K\beta$
Co	Ni $K\beta$
Ni	none

Figure 3.49. Range of secondary fluorescence of Fe $K\alpha$ by Ni $K\alpha$ in an alloy of composition Ni–10%Fe, $E_0 = 20$ keV. The innermost semicircle shows the extent of direct electron-excited production of Ni $K\alpha$ and Fe $K\alpha$ by the beam electrons.
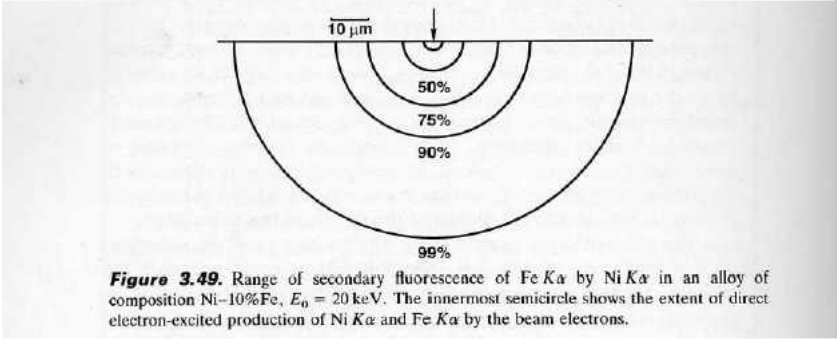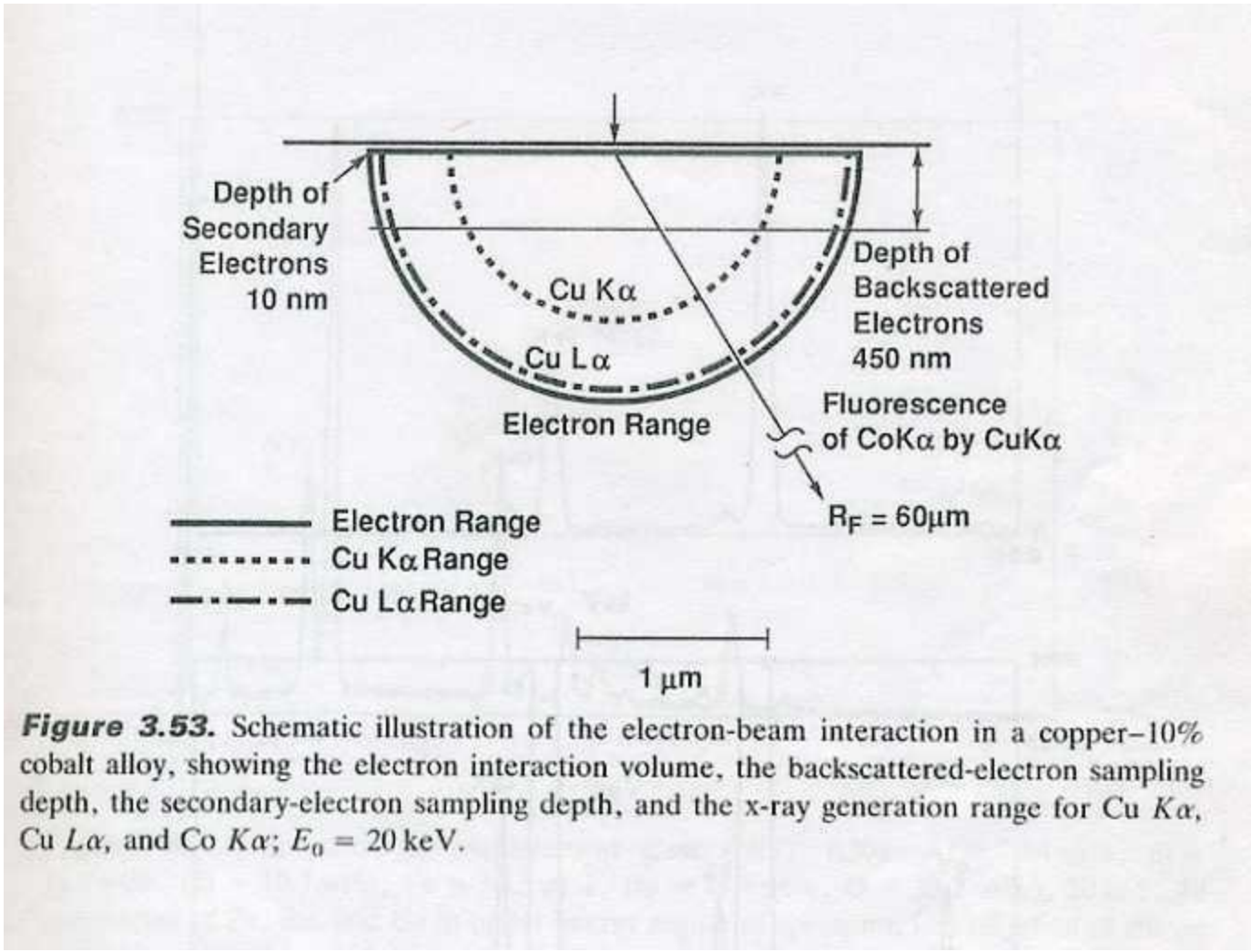
Figure 3.53. Schematic illustration of the electron-beam interaction in a copper–10% cobalt alloy, showing the electron interaction volume, the backscattered-electron sampling depth, the secondary-electron sampling depth, and the x-ray generation range for Cu $K\alpha$, Cu $L\alpha$, and Co $K\alpha$; $E_0 = 20$ keV.
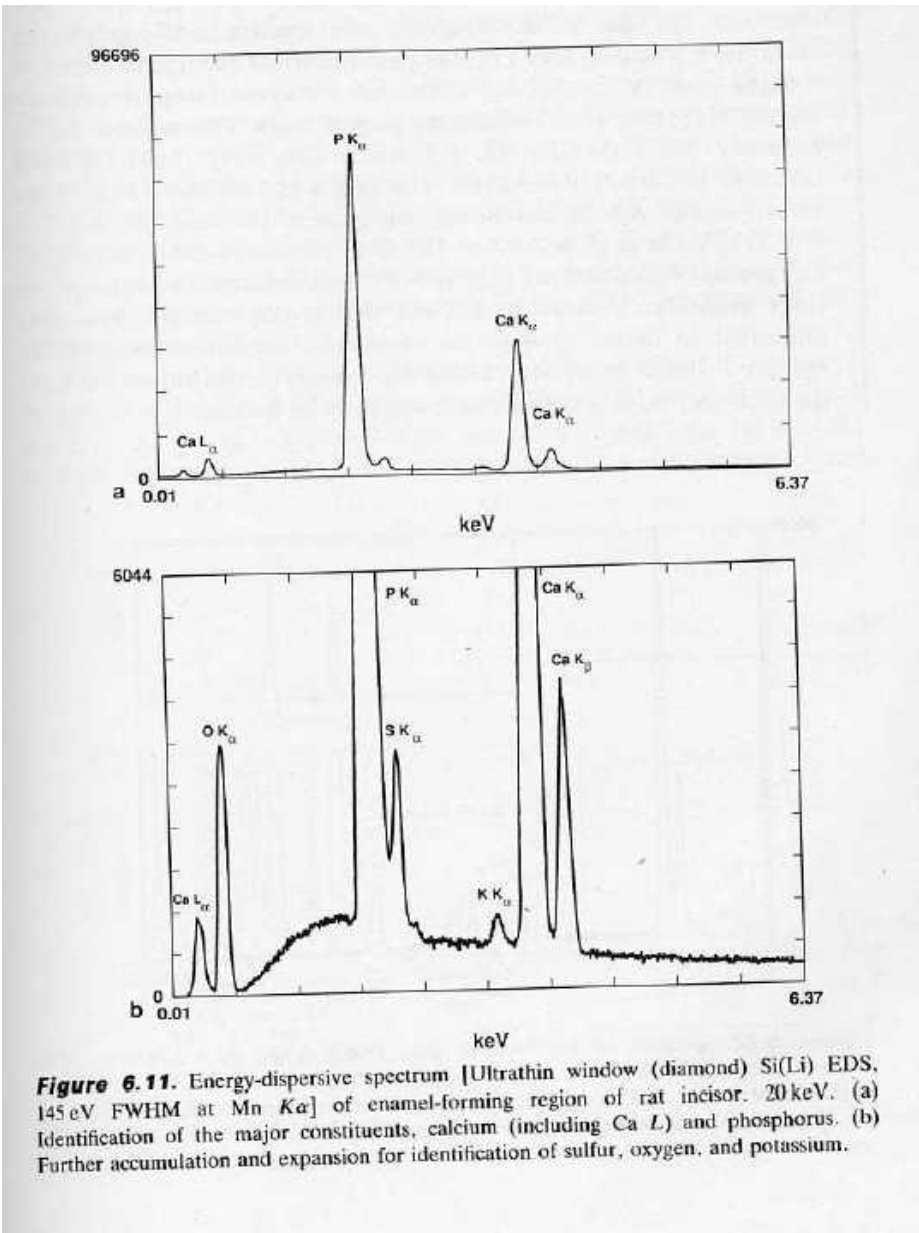
Figure 6.11. Energy-dispersive spectrum [Ultrathin window (diamond) Si(Li) EDS, 145 eV FWHM at Mn $K\alpha$] of enamel-forming region of rat incisor. 20 keV. (a) Identification of the major constituents, calcium (including Ca L) and phosphorus. (b) Further accumulation and expansion for identification of sulfur, oxygen, and potassium.

Figure 6.12. Spectrum of multielement glass (NIST K309: Al = 7.94 wt%, Si = 18.7 wt%, Ca = 10.7 wt%, Fe = 10.5 wt%, Ba = 13.4 wt%, O = 38.7 wt%), 20 keV. Identification of Fe, Ba, and Ca in upper energy region of spectrum; identification of silicon, aluminum, iron-L, and oxygen in lower energy region. (Note: oxygen is a major constituent, but its low energy peak is highly absorbed in the specimen.)
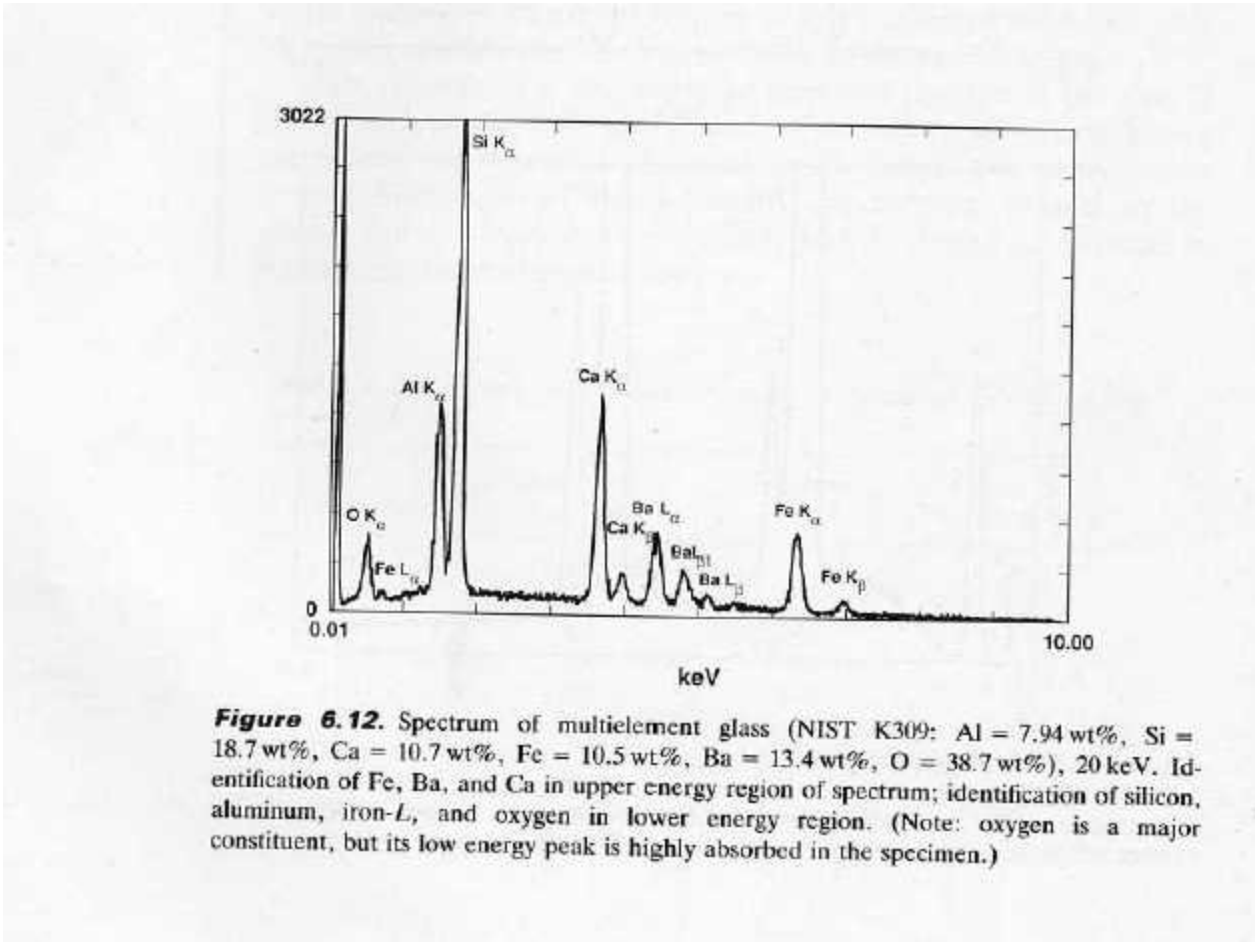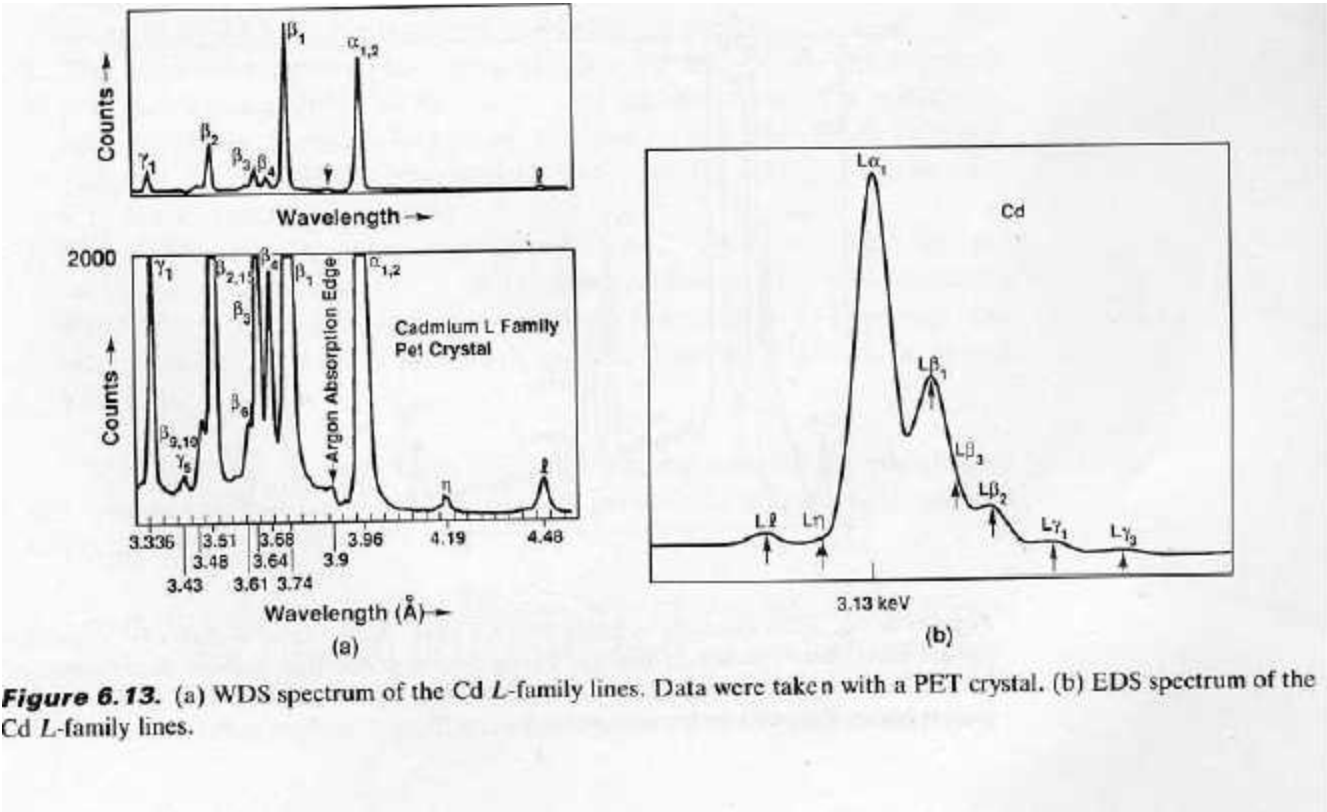
Figure 6.13. (a) WDS spectrum of the Cd L-family lines. Data were taken with a PET crystal. (b) EDS spectrum of the Cd L-family lines.
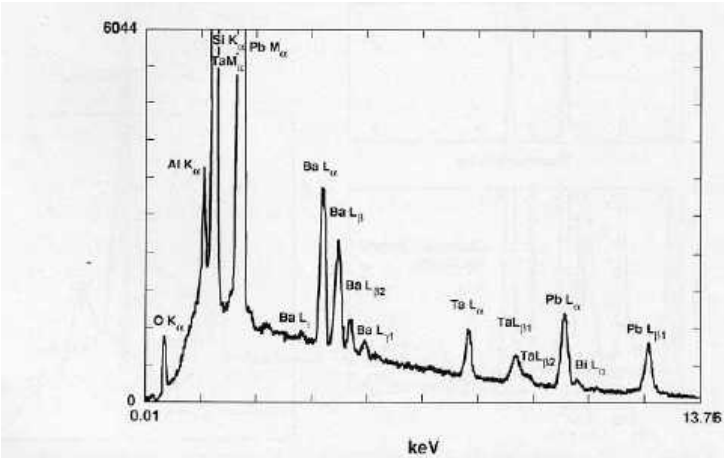
Figure 6.14. EDS spectrum of heavy-element glass. X-ray energy 0–20.0 keV; expanded vertical scale. Identification of Pb, Ta, Ba, and Si as major constituents; identification of minor peaks for Bi, Al, and O. (Note: oxygen is a major constituent, but its low energy peak is highly absorbed in the specimen.)
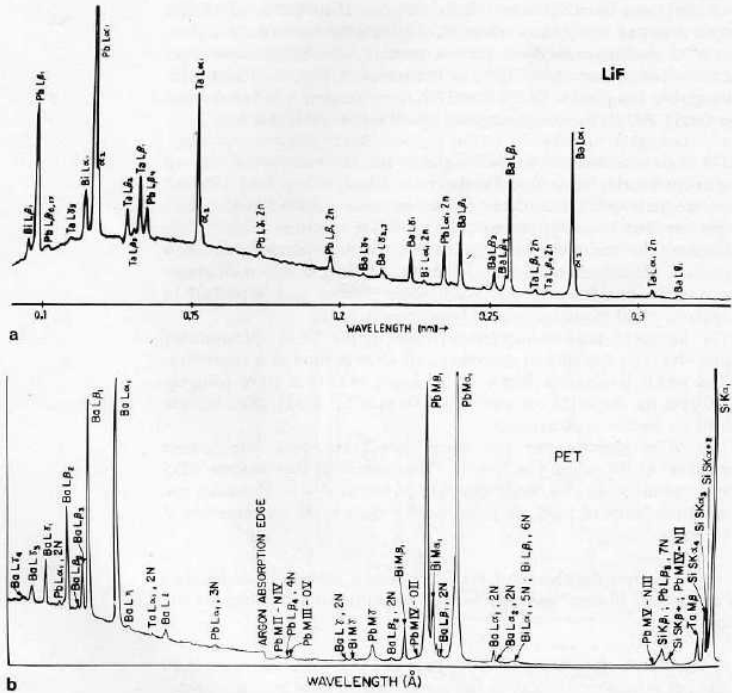
Figure 6.15. WDS spectra of the same heavy-element glass as in Fig. 6.14. (a) LiF spectrum. (b) PET spectrum. (c) AP spectrum. (d) lead stearate (OdPb) spectrum.

X-38 X-RAY ANALYSIS [ERRORS AND ACCURACY]

N_{B_1} — Energy — N_{B_2}
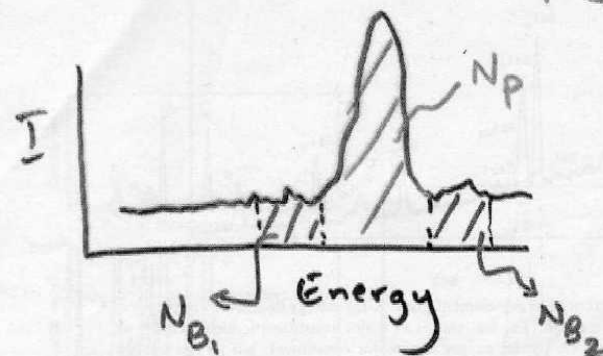
N_{P-B} = Intensity beneath peak = $N_P -$

$[N_{B_1} + N_{B_2}]$

$= N_P - N_B$

$$\sigma^2_{P-B} = \sigma^2_P + \sigma^2_B = N_P + N_B$$

where σ = standard deviation

$= \sqrt{No. \ of \ counts}$

$$\sigma_{P-B} = (N_P + N_B)^{1/2}$$

$$\sigma_{P-B} / N_{P-B} = \frac{(N_P + N_B)^{1/2}}{N_P - N_B}$$

QUANTITATIVE ANALYSIS
ZAF METHOD

1. Z atomic number effect

➤ Penetration of electron beam depends on composition! (e.g.,) $t_{Cu-Au} < t_{Cu}$

➤ Energy of electron is not divided among elements in proportion to their weight fraction

e.g., As Z ↑, No. of x-rays generated ↑

But number of backscattered electrons [which do <u>NOT</u> lead to x-rays] also ↑

2. Absorption 'A'

Generated x-rays are absorbed IN sample before leaving surface
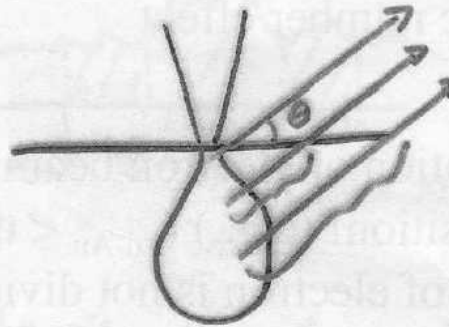
Absorption depends on distance travelled, x-ray energy & absorbing material

3. Fluorescence, 'F'

In a Cu-N_1 alloy, Cu X-rays can excite N_1 x-rays, i.e., $I_{Cu}\downarrow$, $I_{N1}\uparrow$

ZAF corrections assume a composition & calculate Intensities (after correcting for Z,A,F). These are compared with OBSERVED intensitites. Process is repeated with a better guess of composition.

Assumptions :

➤ Material has homogeneous comparison!
➤ Crystallinity & channeling absent
➤ "Infinite" sample [errors for pocuring thin films]
➤ All elements __must__ be specified [if oxides, carbides, ….. Then the stoichiometry must be specified if these light elements cannot be detected]
➤ Data for ZAF available? (Unreliable for light elements)

QUANTITATIVE X-RAY ANALYSIS (ZAF)

1. The 'Z' correction involves 2 terms: as the matrix changes, so does backscattering efficiency. Thus, electrons generate Al x-rays from deeper in the sample when the matrix is Al than when the matrix is Au. The other term is the stopping power. Lower 'Z' leads to more efficient energy loss, thereby removing the electrons power to cause ionisation. These 2 effects partly cancel.

2. The 'A' correction involves a product of the functions that relate x-ray generation with depth and x-ray absorption on the way out.

3. Fluorescence is important only if the x-ray energy is within~5 keV of the absorption edge of the element which can fluoresce.

4. Standardless analysis assumes many things which are suspect. These include detector efficiency (degrades over time, and dependent on x-ray energy), ionisation cross sections and fluorescence yield (poorly known for low energy x-rays and L/M families), backscattering (well known), absorption (not well known below 3 keV).

QUANTITATIVE X-RAY ANALYSIS (ZAF)

5. Relative variations in composition across a sample may be reasonably reliable in standardless analysis. For absolute numbers, check that you get the same answer by using different voltages and different families of lines. But for real reliability:

6. Use standards. Acquire spectra from elemental or stoichiometric mineral standards at the same conditions as the unknown. (Make sure that the standards are reliable!)

7. If the sample is not polished and semi-infinite, errors arise, e.g., in thin films (supported or unsupported), powders (embedded or otherwise) and rough surfaces, because the ZAF method presupposes these 2 features.

8. Best to analyse at normal incidence. Today's software can account for changes in backscattering with glancing incidence, absorption, etc., but these corrections are subject to their own uncertainties. Avoid them if you can!

Low Voltage EDS

- High probe current with small spot sizes
- Low kV BSE imaging
- Low element peak separation
- High magnification bulk EDX analysis
- Small interaction volume / High spatial resolution
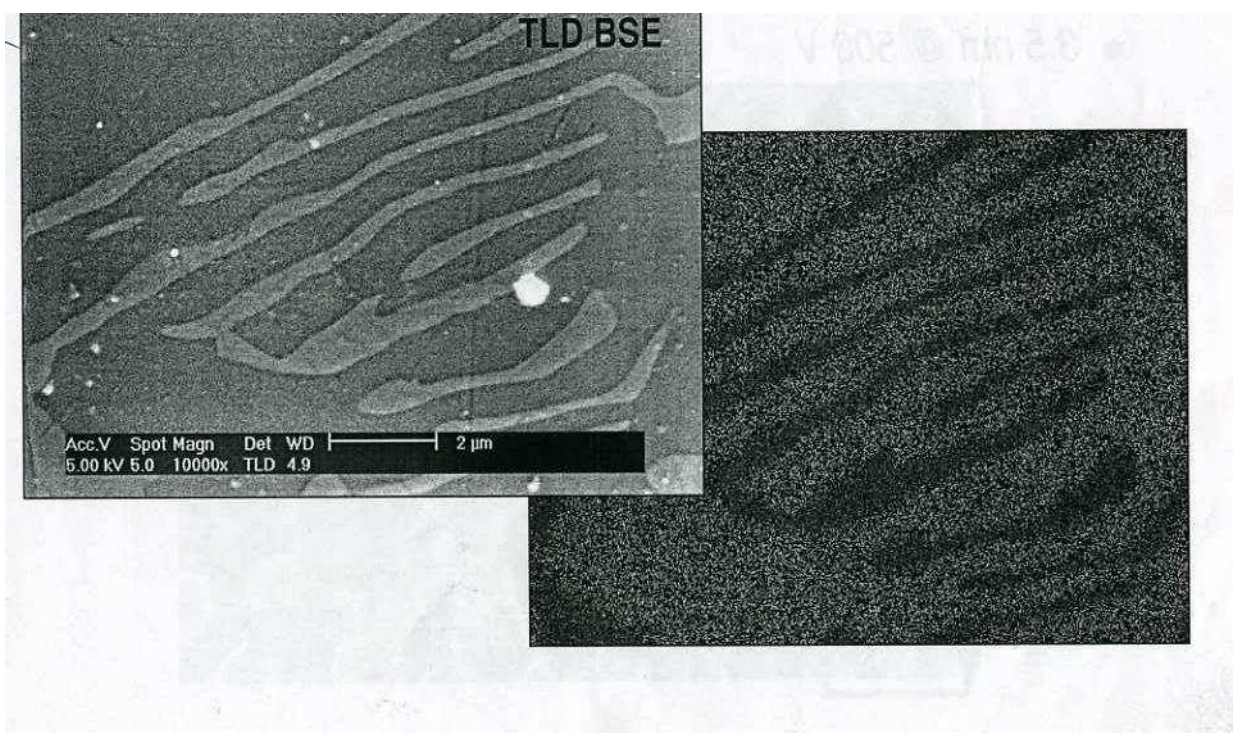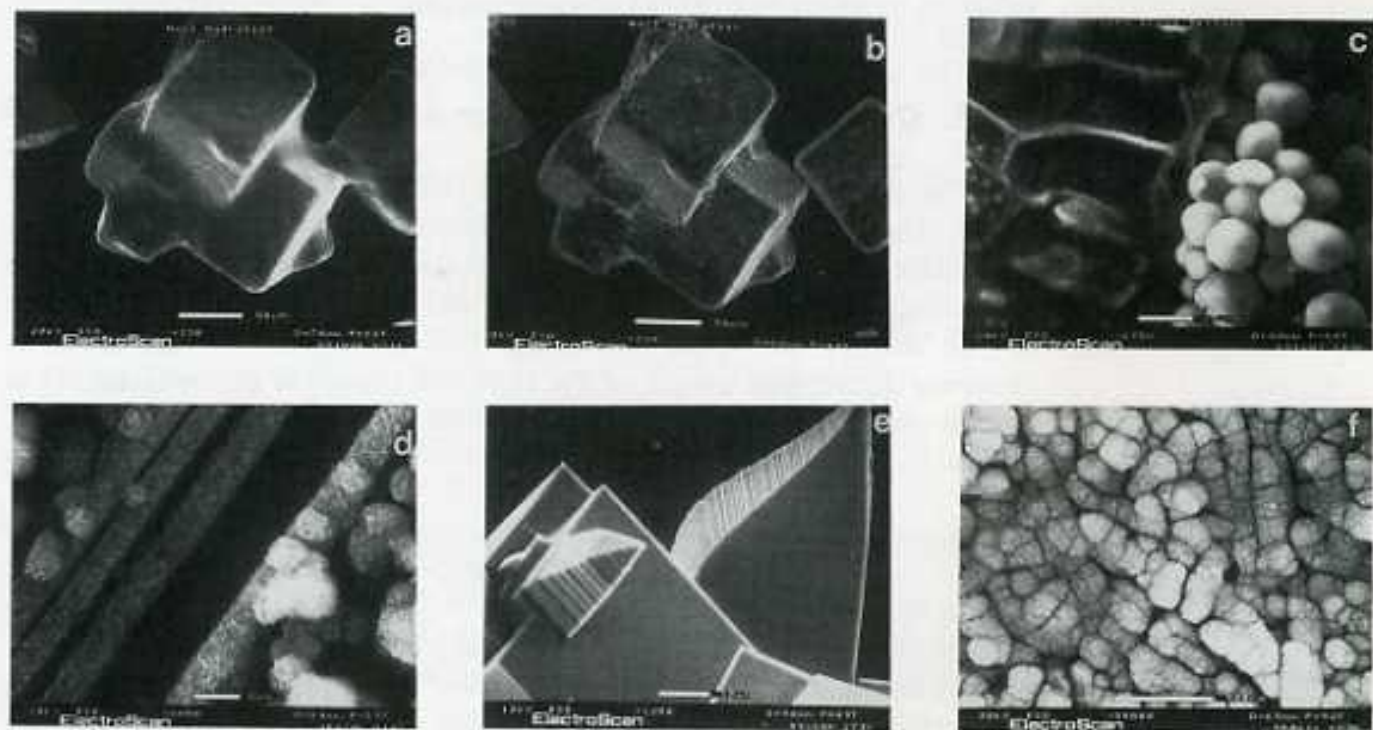
Figure 12.1. Images taken using an environmental microscope. (a) Sodium chloride crystals in wet state: 20 keV, 1600 Pa, magnification bar = 50 μm. (b) Sodium chloride crystals in dry state: 20 keV, 533 Pa, 10 °C, magnification bar = 50 μm. (c) Corn (*Zea mais*) cross-section: 12 keV, 1040 Pa, 10 °C, magnification bar = 20 μm. (d) Solvent-etched polymer: 20 keV, 706 Pa, magnification bar = 2 μm. (e) Potassium chloride crystals grown at 600 °C: 12 keV, 653 Pa, magnification bar = 10 μm. (f) Resolution test specimen of gold-coated oxide particles: SE, 30 keV, 1226 Pa, magnification bar = 500 nm. [Pictures courtesy of Danilatos (1991).]

Figure 4.66. Application of the environmental SEM to a dynamic crystallization experiment. Lead and potassium chloride were heated together in water vapor, and the process was followed with continuous recording on videotape. (a) 650 °C, crystals of potassium chloride grown during the heating cycle. (b) 890 °C, lead oxide film on surface of molten lead, with only traces of crystals of potassium chloride remaining after vaporization. (Example courtesy of the Electroscan Corp.)

Figure 4.66. (Continued).

ELECTRON CHANNELING

Between 3,4 : Poor
or **1, 2** channeling

Between 2,3 : Good channelling

- Diffraction occurs over a range of θ
- Angle between incident & diffracted beams = 2
- $0 < \theta < \theta_B \Rightarrow$ poor channeling
  $\theta > \theta_B \Rightarrow$ good ..

Incident beam

$2\theta_B$
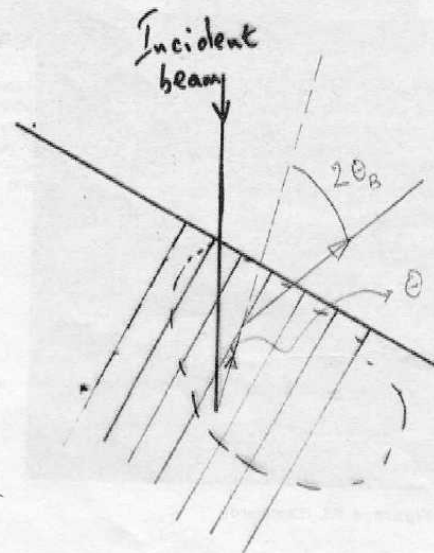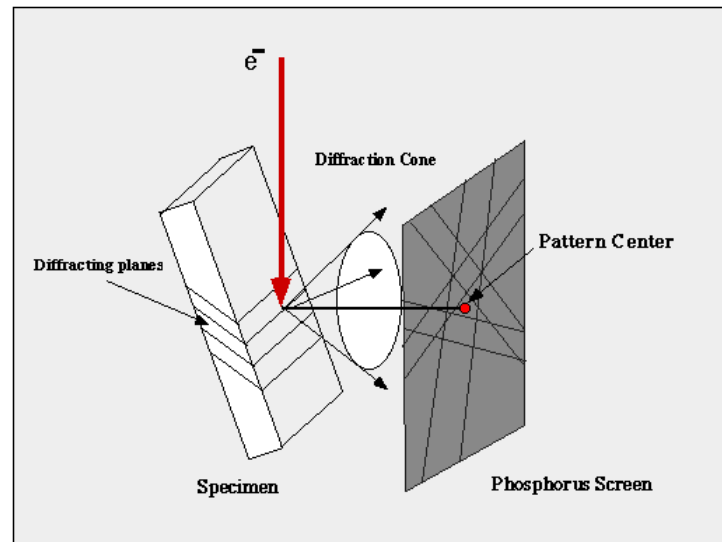
Schematic of the diffraction cone and pattern formation
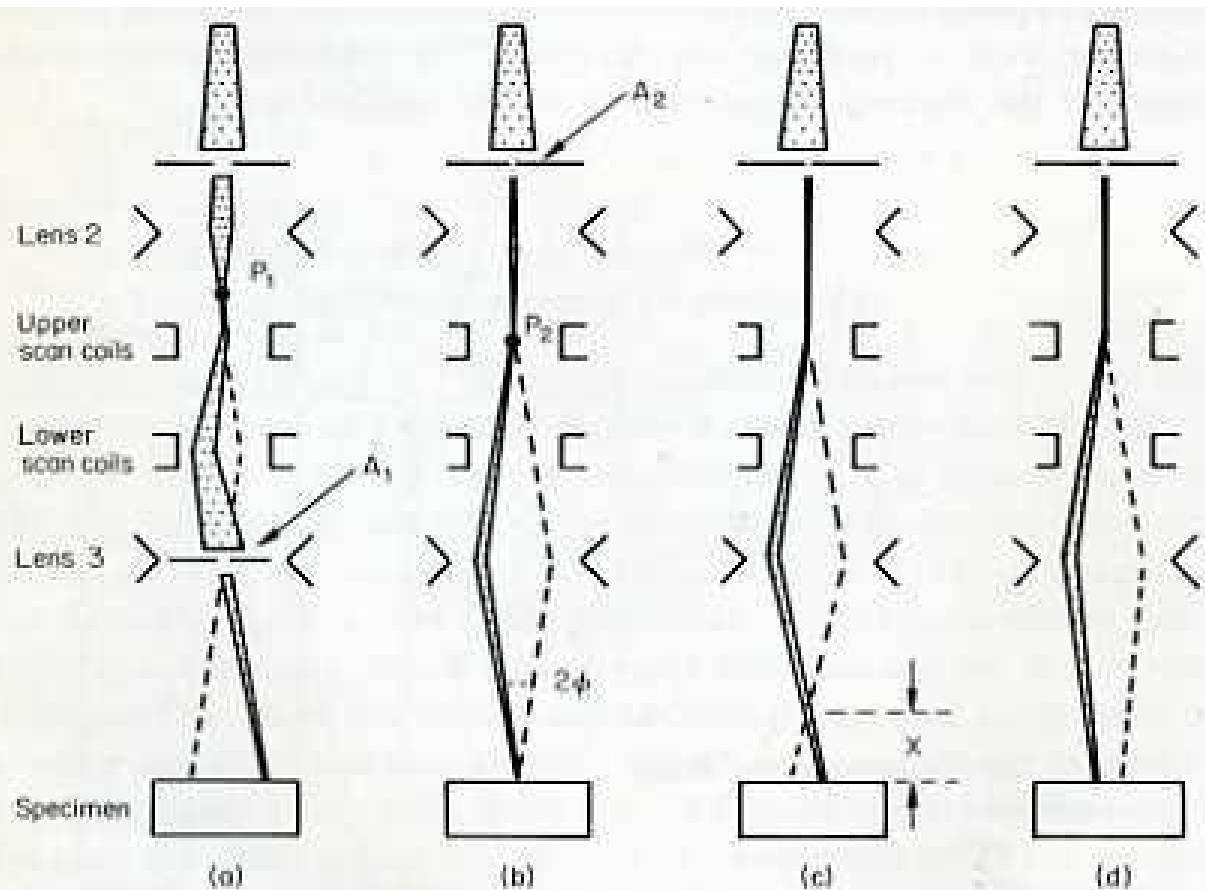
FIG. 7.3 Scanning modes. (a) Topographic scanning mode; (b), (c), and (d) selected area mode. (Joy and Booker 1971. Courtesy of J. Phys. E.)

- *Investigation of YBCO HTS on RABiTs Ni Substrate*
- *with Cerium Oxide and Yttrium Stabilised Zirconia*
- *buffer layers using Montage Large Area Crystal*
- *Orientation Mapping*

Electron image of Nickel alloy substrate showing area analysed

COM for sample normal showing highly aligned [001] structure

Misorientation map showing grain boundaries in the ranges 1-3º, 4-6º & 7-9º

Misorientation histogram showing a gaussian distribution of grain size peaked at 6º - 7º

True Grain ID map with **2º** grain boundary threshold

Boundary threshold set True Grain ID map with **4º** grain boundary threshold set.

True Grain ID map with **5º** threshold set.

True Grain ID map with **6º** threshold

True Grain ID map with **9º** threshold

Figure 1. Large area Montage mapset showing predominant [001] alignment and grain boundaries with Histogram. The True Grain ID sequence shows the distribution of grains

Results

All Pole Figures and Inverse Pole Figures plotted for the 'Sample Normal' i.e.., perpendicular to the surface of the materials.
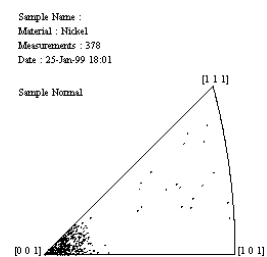
Inverse Pole Figure showing 'ab' in plane alignment
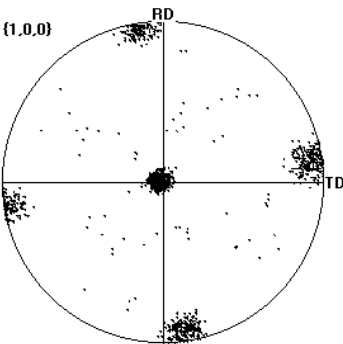
Pole Figure showing 'c' axis alignment with the sample normal (centre of the plot$)$

Figure 3 Inverse Pole Figure and Pole Figure, showing highly textured structure of the Nickel substrate tape with excellent 'ab'

in plane and c axis alignment.

Sample 2 YSZ deposited on top of CeO
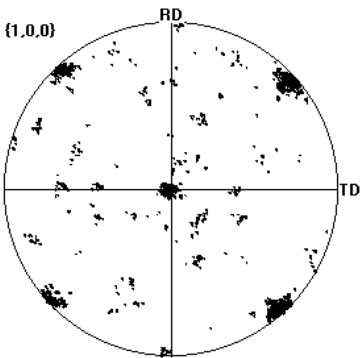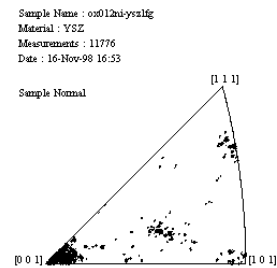
Figure 4 Showing the texture of the YSZ layer, with good rotational alignment, rotated by 45° compared with the Ni substrate.

The inverse pole figure shows 'ab' in plane alignment and the pole figure shows the 'c' axis aligned with sample normal at the centre of the plot.

Investigation of Titanium Containing 'Electrical' Steels for use in Power Generation and Distribution

[001] [101] [111]
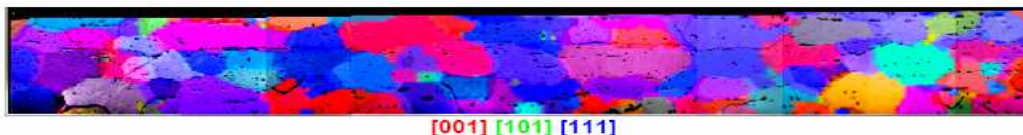
Figure 1. Montaged COM's of a cross section through a 'good' low Ti content steel, showing grain orientations and evenly distributed large grain structure.

50um

[001] [101] [111]
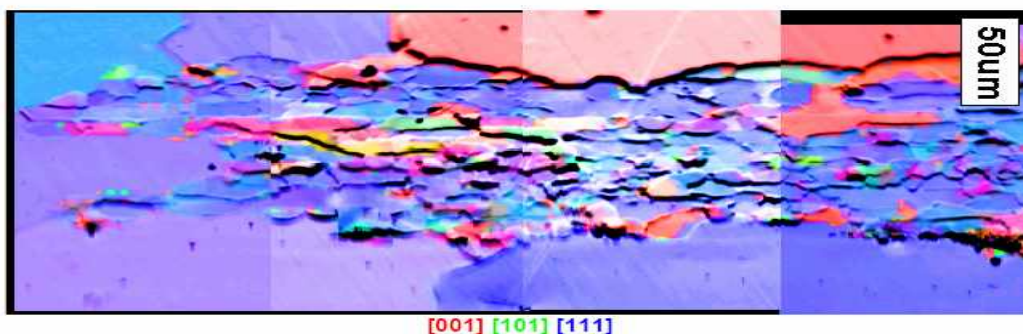
Figure 2. Enlargement of montaged COM's of a cross section through a 'bad' high Ti content steel, showing the grain orientations and large surface grains separated by small central grains.

Introduction

'Electrical' Steels is a term applied to soft Ferro-magnetic steels intended for use in the power generation and distribution industry. The magnetic properties, rather than electrical properties, is the prime consideration and this is known to be controlled by grain size, and grain orientation. Composition has a controlling influence and the presence of titanium in particular, is important.

The magnetic permeability of strip and sheet to be made into laminations for motor, generator and transformer cores is critical in determining the efficiency of such electrical devices. In use, significant amounts of energy may be wasted due to unnecessary heat losses, with accompanying financial losses as well as environmental considerations.

EBSD was used to investigate the influence of titanium in controlling the grain size, local grain orientations, and to characterize predominant grain boundaries in order to account for the observed variation in properties of the finished product. This report predicts the mechanism by which the presence of titanium influences those properties.
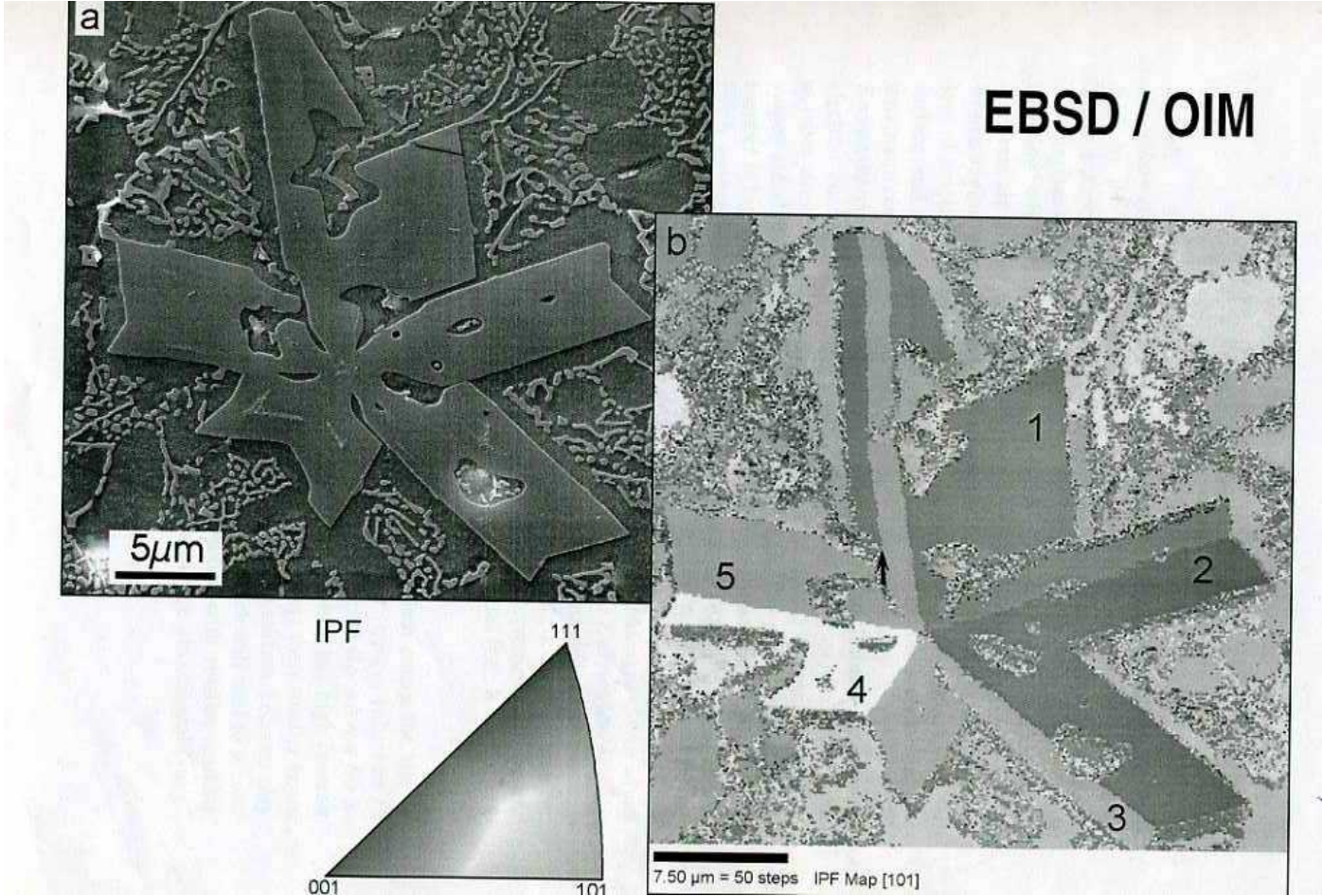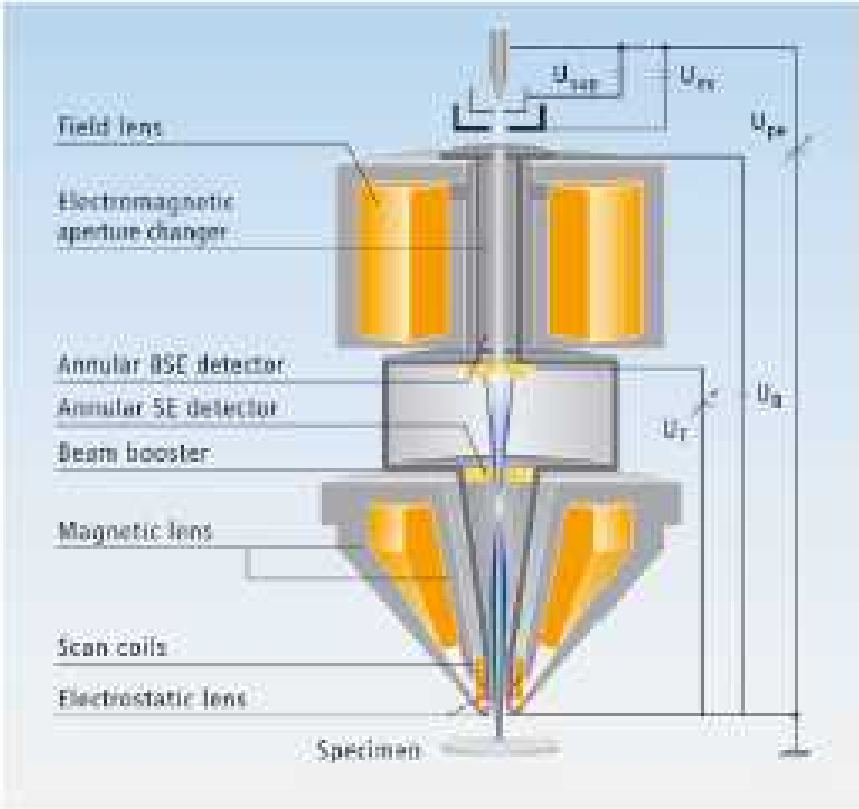
Fig. 1: Cross section of the Gemini electron optical column utilised in the Ultra FESEM.
Uex – extractor voltage of first anode
UPE – primary beam voltage
UB – booster voltage
UF – EsB filtering grid voltage
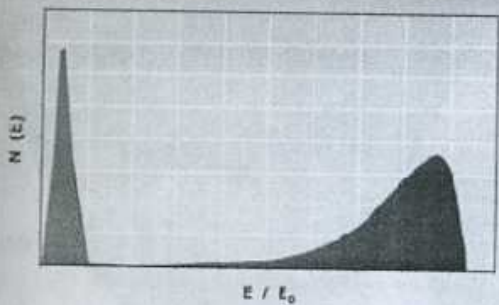
Energy distribution of electrons emitted by sample
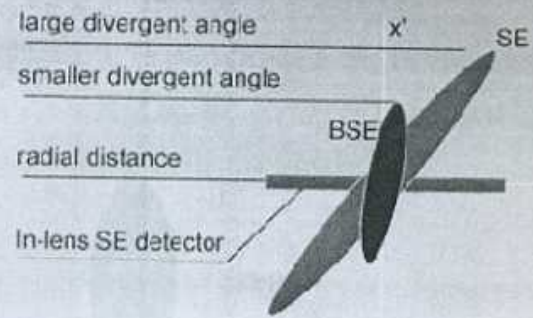
Backscattered (high energy) electrons go ~ straight up column. Secondaries diverge
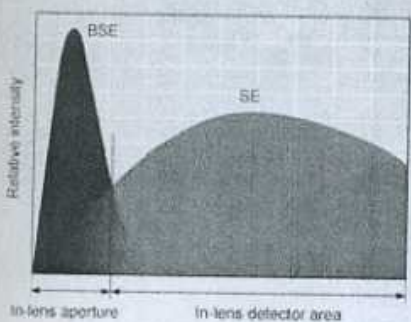
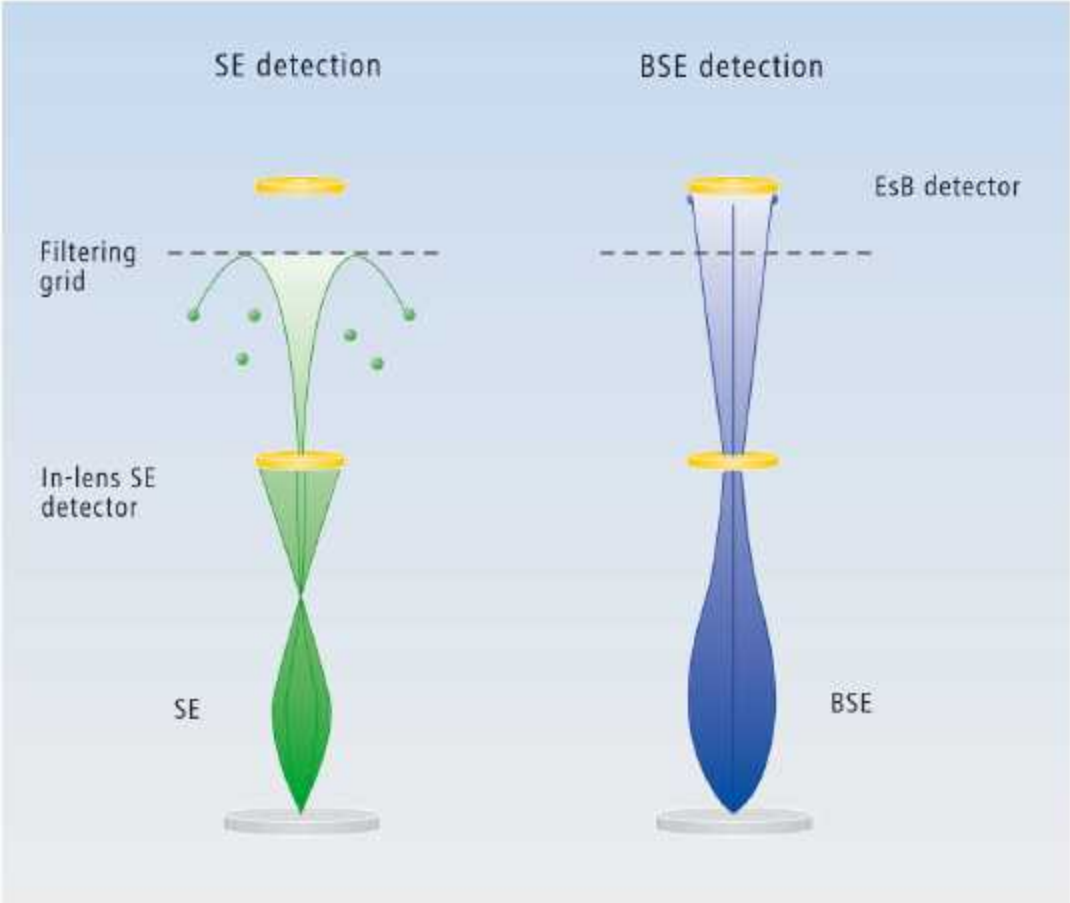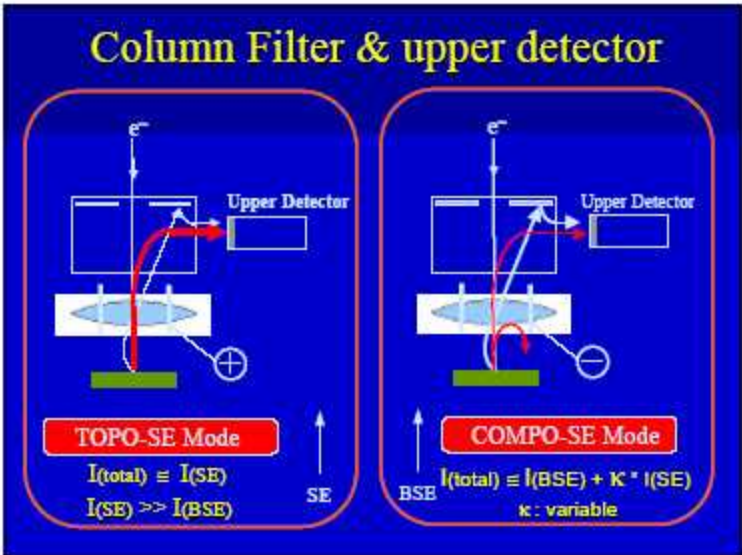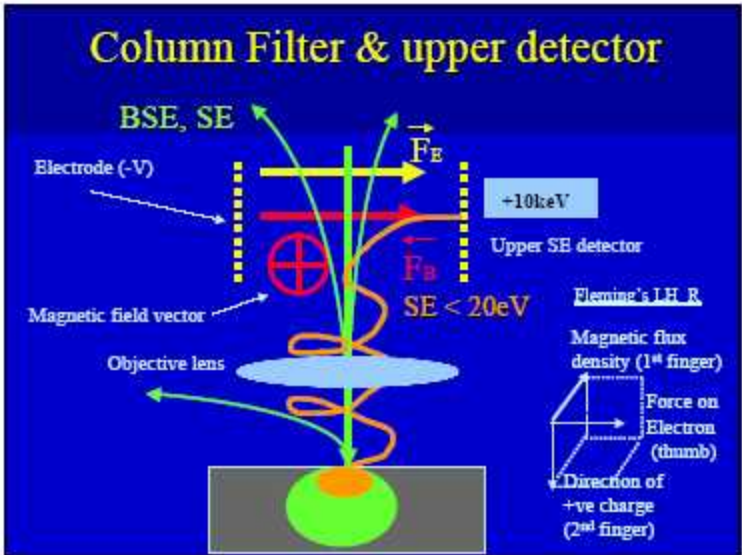An annular detector picks up secondaries and allows BSE to go through to another detector where a bias eliminates the few SE that get in
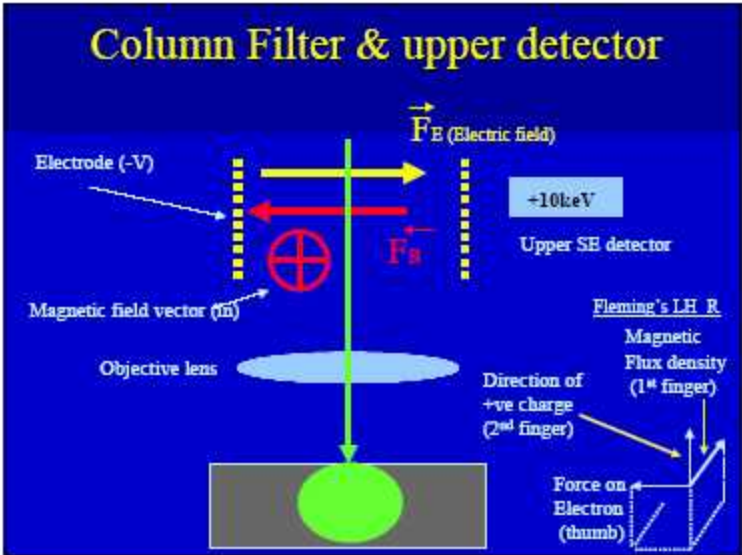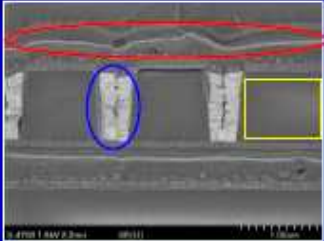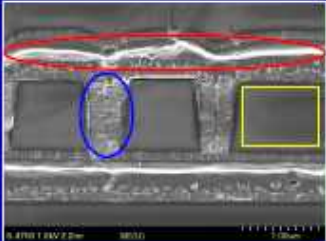
Fig. 7: The SEs (green) are projected onto the high efficiency In-lens detector and the BSEs (blue) are guided onto the integrated EsB detector.
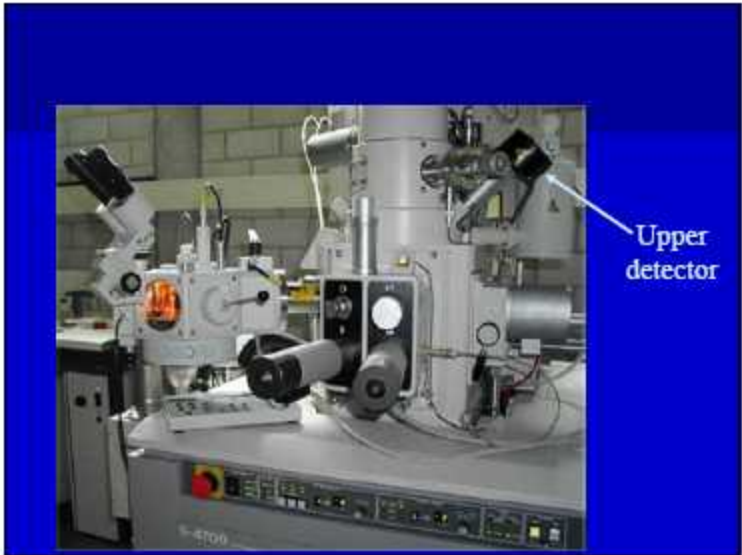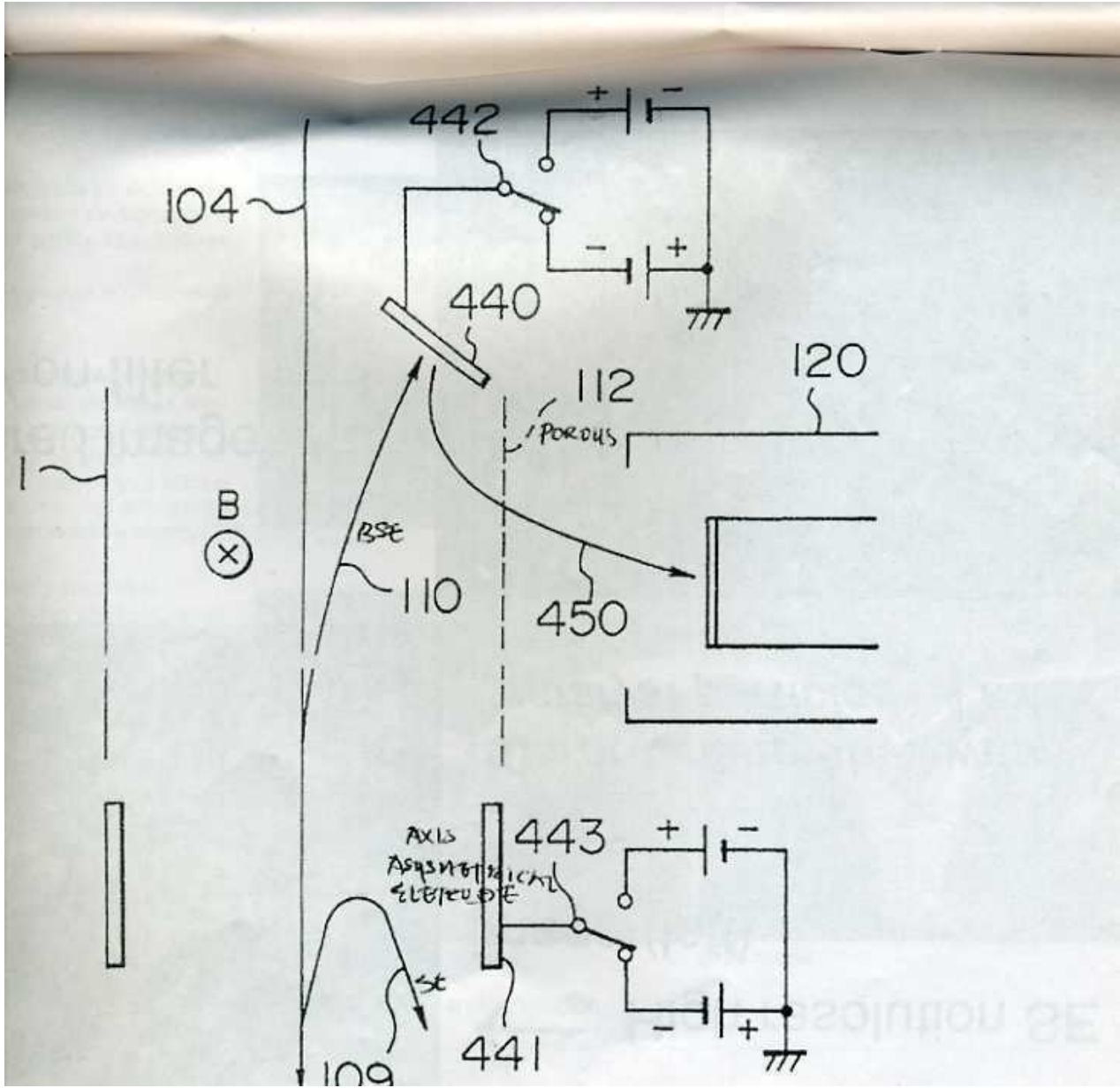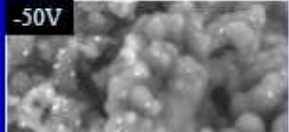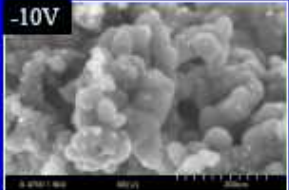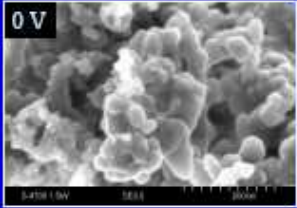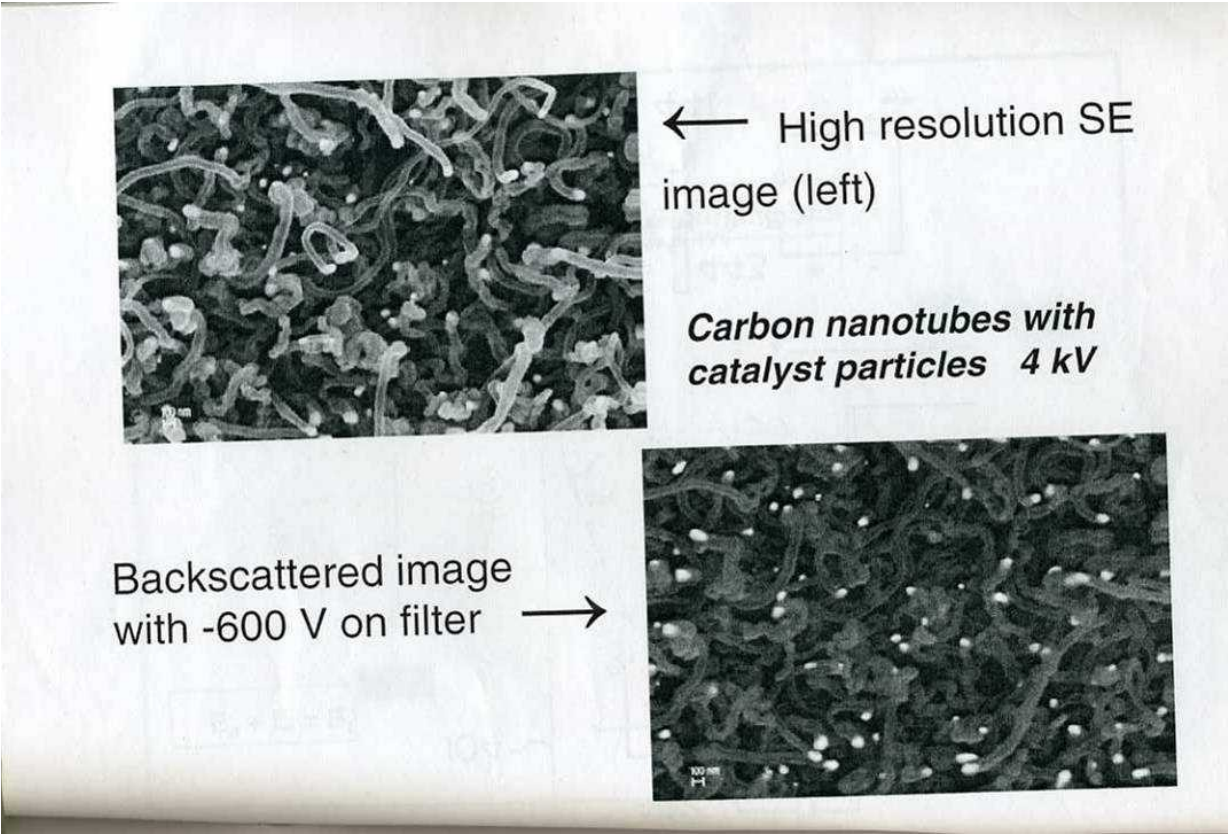
442

104

440

112

POROUS

120

B
⊗

BSE

110

450

AXIS

ASYMETRICAL
ELECTRODE

443

st

441

109

← High resolution SE image (left)

Carbon nanotubes with catalyst particles 4 kV

Backscattered image with -600 V on filter →

SE and BE (backscattered) modes show respectively topographic contrast (enhancement of soft Al edge) and atomic number contrast (W versus Al). The Sb mode superimposes a little BS signal on the mainly SE signal, allowing you to see some atomic number differences that help to delineate the layers. The Bs mode is the reverse: a little topography is seen on a primarily Z-contrast image.
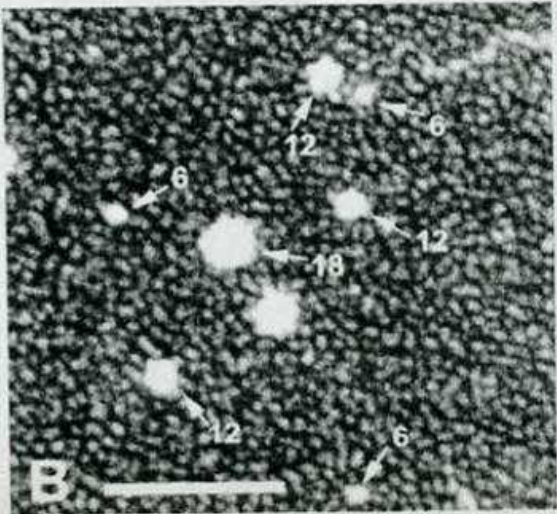

Cross section of semiconductor.
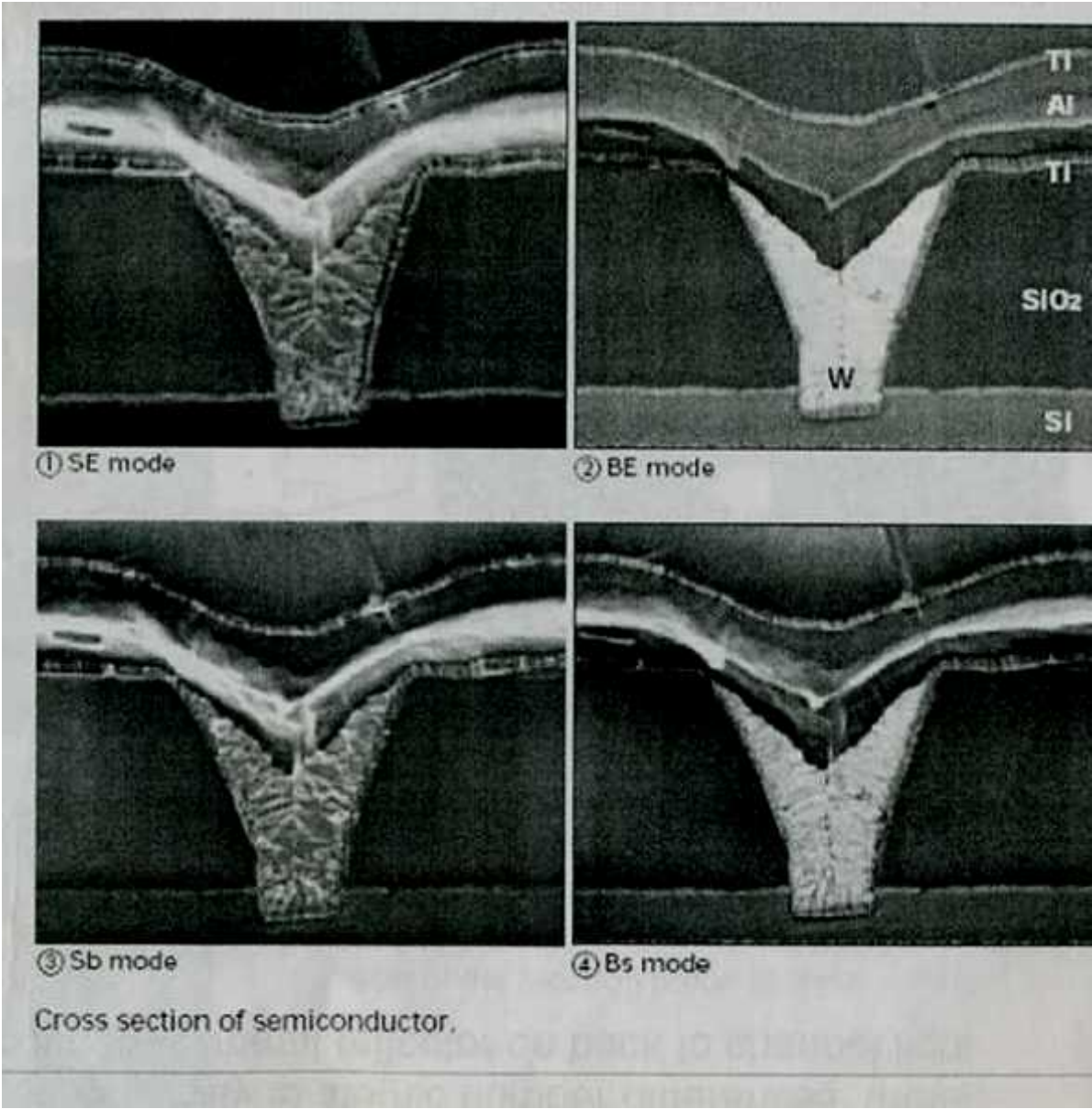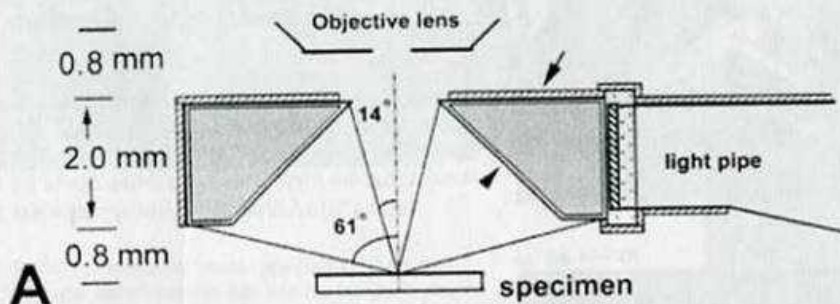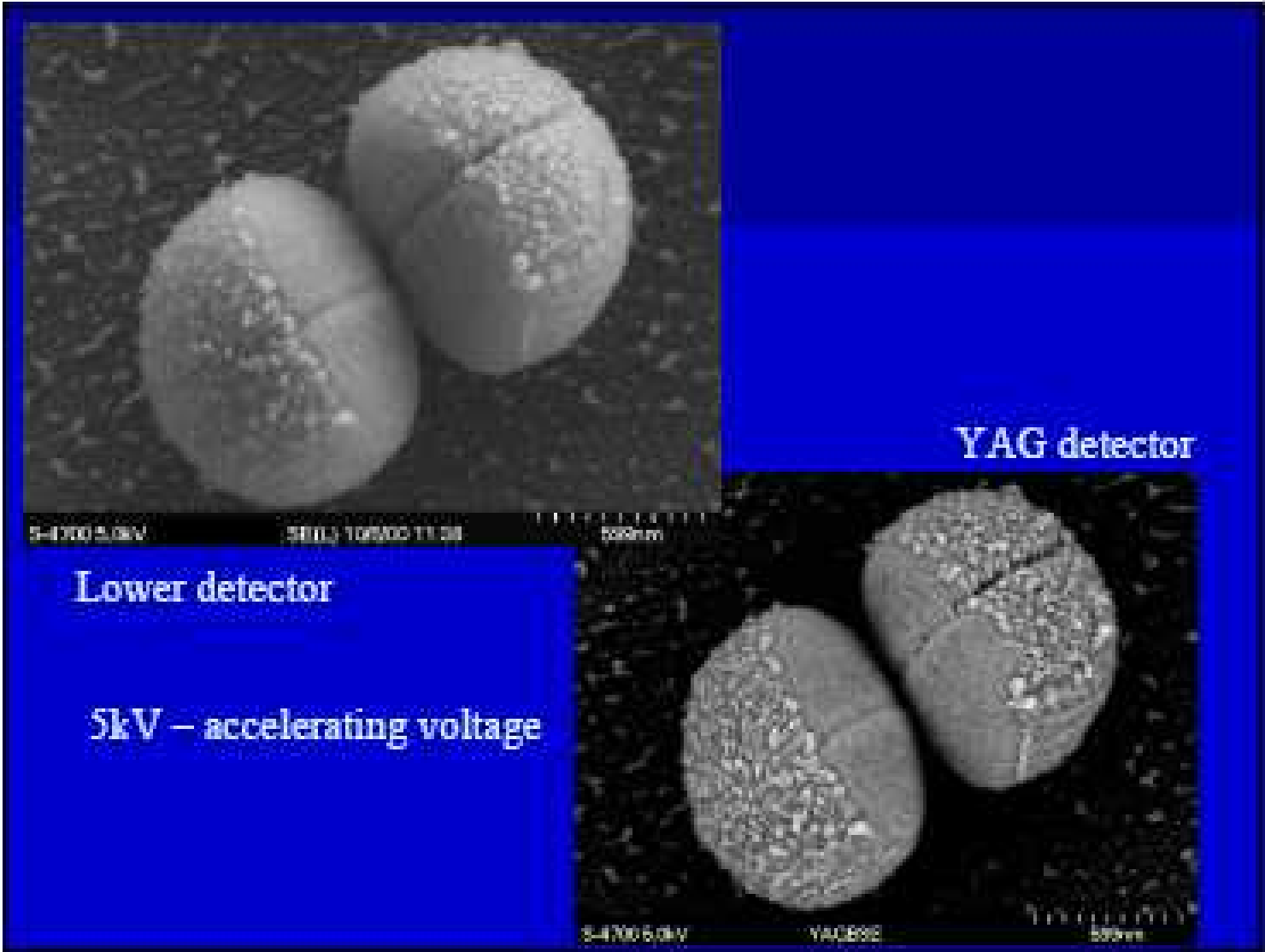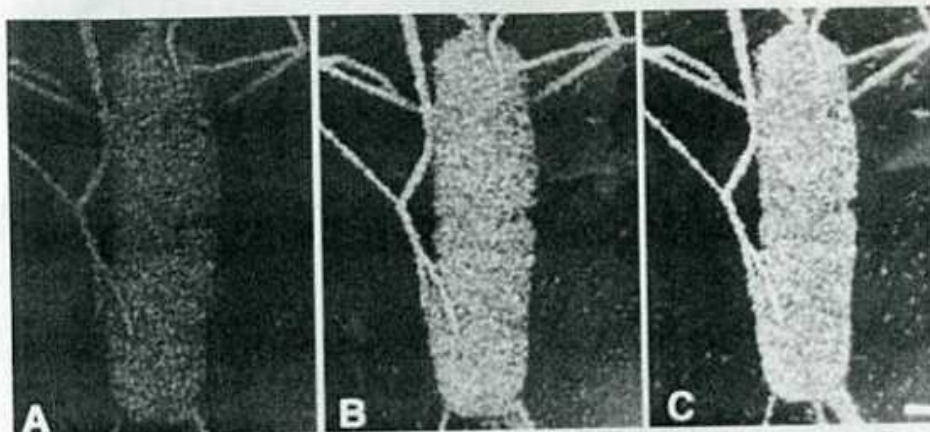
BSE Signal Detection
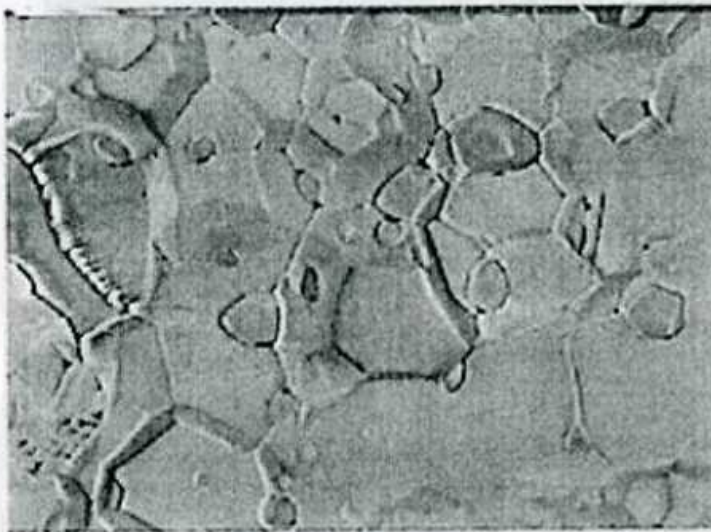
SE
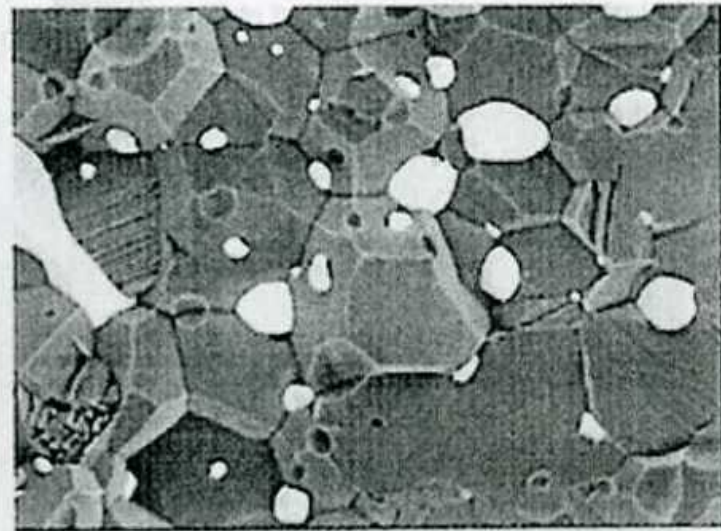
SE+BSE

HV   : 2kV
Mag   : 20kX
Sample   : Al/Ni

YAG scintillator for highest sensitivity to atomic number differences: metal oxide coating to stop secondaries, metal reflector on back to channel light into light pipe
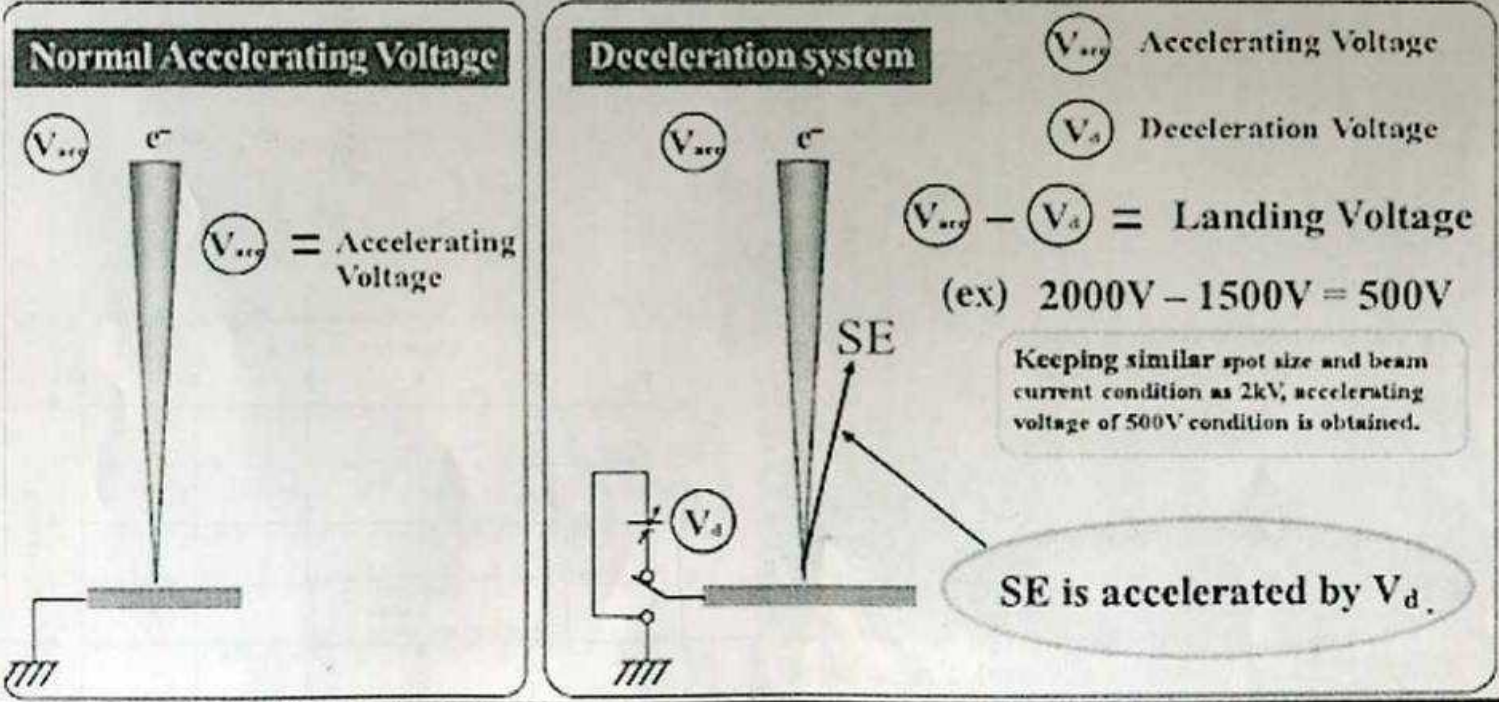
(A–C) BSE images of the same *P. mirabilus* immunolabelled with 12-nm colloidal gold. And imaged at 1.6 keV (A), 1.8 keV (B) and 2.0 keV (C). Shape of cell and flagella are detectable by topographical contrast in A, but in B and C, the immunogold can be seen by atomic number or compositional contrast. The threshold for atomic number contrast by BSE imaging is approximately 1.8 keV. Scale bar = 200 nm.
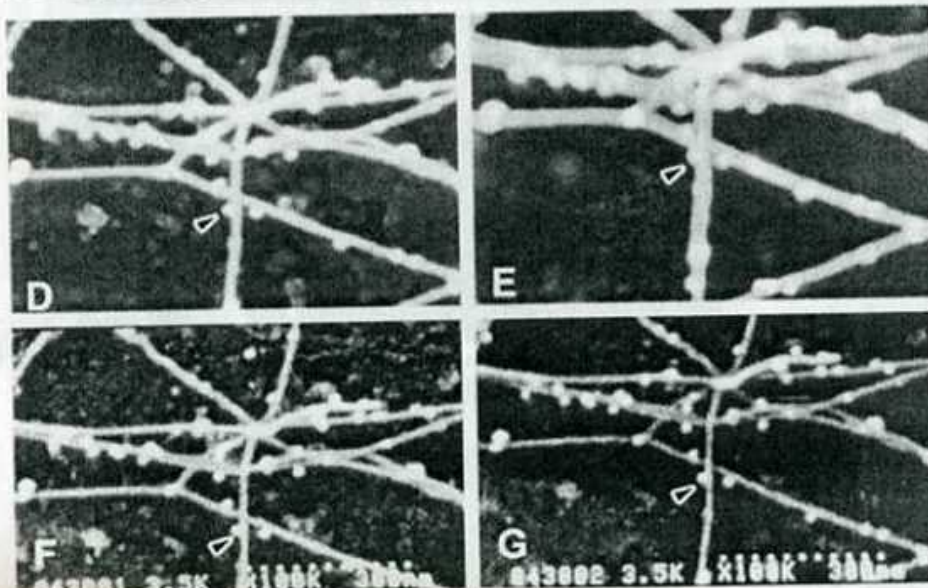
SE (D,E) and BSE (F,G) imaging of bacterial flagella immunolabelled with 12-nm gold. D and F were collected at 0 time and E and G were collected after 3 min of continuous exposure to the beam at 100 000× at 3.5 keV. Exposure of flagella to electron beam for 3 min produces contamination of flagellar surfaces (compare E and D) resulting in increased thickness as seen by SE imaging. Examination of the same image by BSE imaging (compare G and F) does not show any sign of contamination due to the higher energy level of the BSE (90% of 3.5 keV) and the transparency of the carbon contamination to these higher energy electrons. Arrowheads in D–G point to same colloidal gold particle

Deceleration

Deceleration technique is well known system to obtain higher resolution by decelerating primary electron beam voltage(V_{acc}) just before landing at the sample. For deceleration negative voltage (V_d : Deceleration voltage) is applied to the sample.
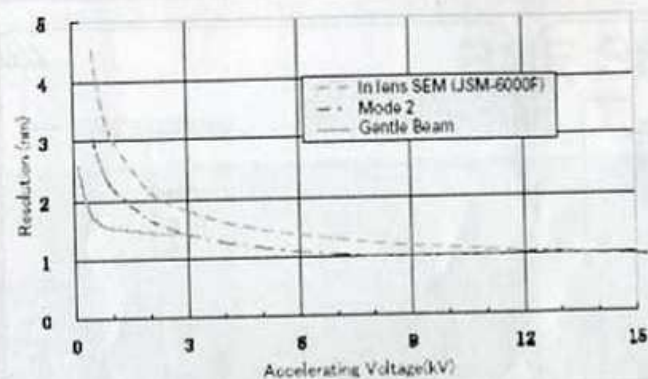
Normal Accelerating Voltage

e^-

V_{acc} = Accelerating Voltage

Deceleration system

e^-

SE

V_d

V_{acc} Accelerating Voltage

V_d Deceleration Voltage

$V_{acc} - V_d$ = Landing Voltage

(ex) 2000V − 1500V = 500V

Keeping similar spot size and beam current condition as 2kV, accelerating voltage of 500V condition is obtained.

SE is accelerated by V_d.

Fig. 11. Accelerating voltage versus resolution.

Mode 2: Accelerating voltage 1 kV

r-filter: Accelerating voltage 1 kV
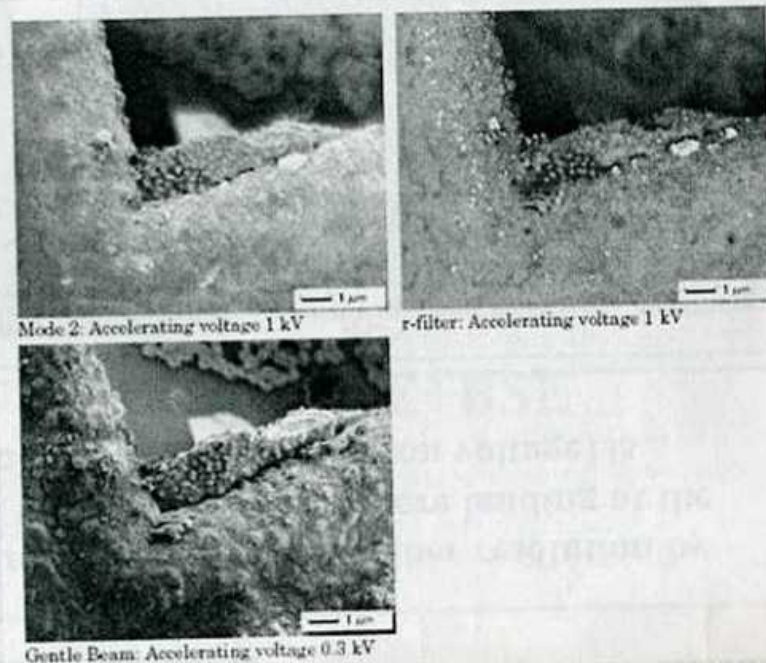
Gentle Beam: Accelerating voltage 0.3 kV

Fig. 12. Comparison of SEM images (mesh). Image obtained through normal observation (mode 2) (top left) and images obtained using the new secondary electron detection systems (top right and bottom). Magnification: ×10,000

Resolution

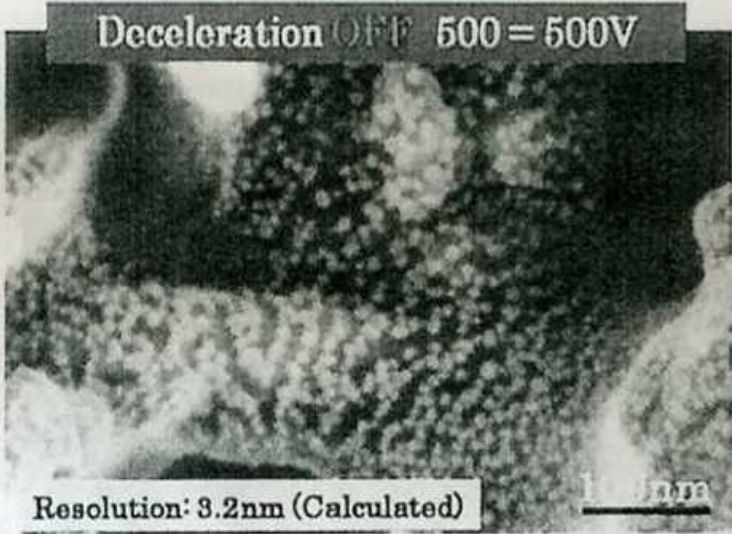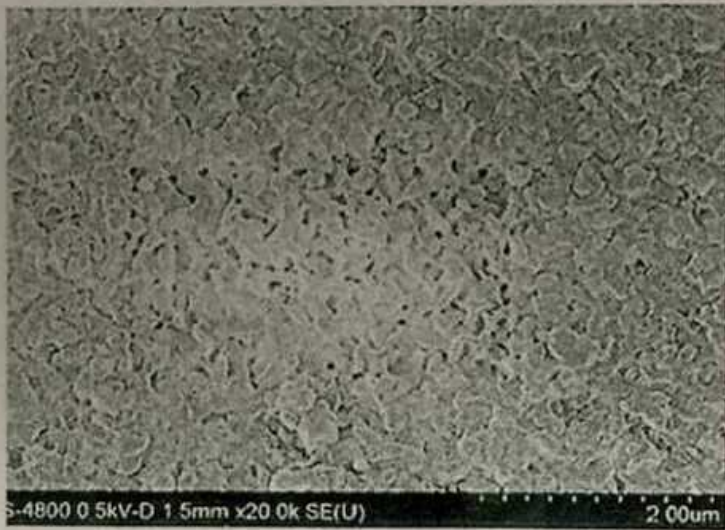**Deceleration OFF 500 = 500V**

Resolution: 3.2nm (Calculated)

Image clarity at 500 volts with a decelerated beam is much better than the image from an initial 500-volt beam. The estimated resolution at 500 volts with beam deceleration is equivalent to the guaranteed resolution of a 1kV beam.

Deceleration ON 2000 – 1500 = 500V

Resolution: 2.0nm
(Estimated)

Deceleration OFF 1kV = 1kV

Resolution: 2.0nm (Guaranteed)
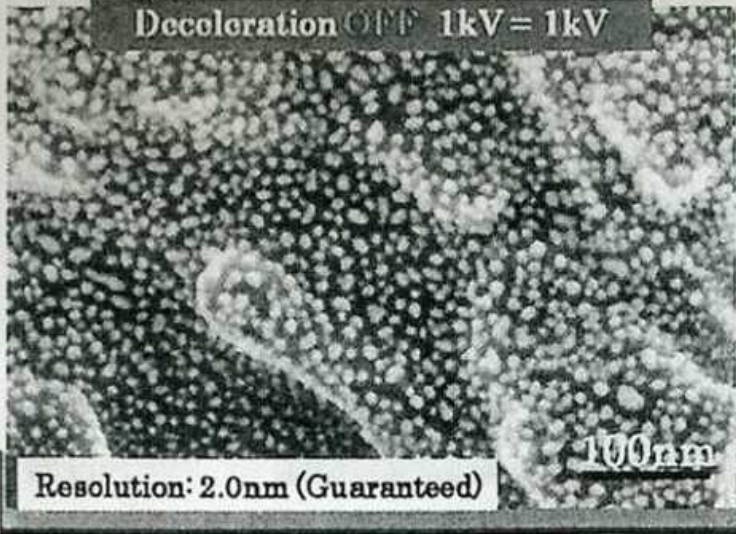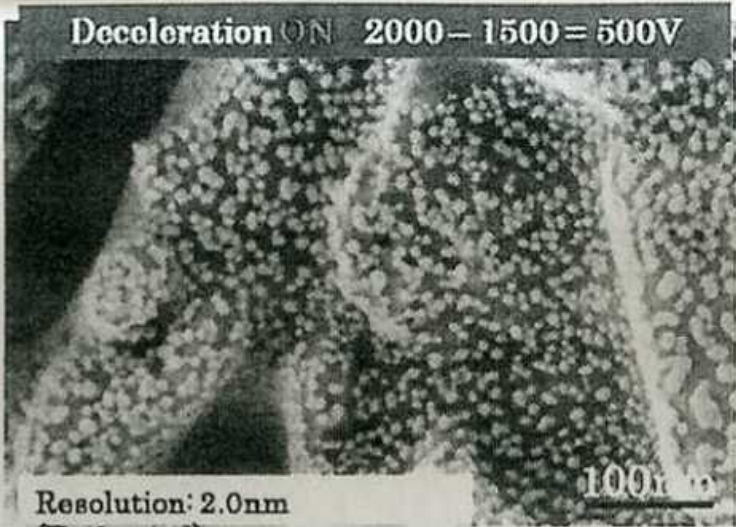
Fluoride Resin

Ultra low voltage imaging reveals a completely different morphology of the fluoride resin.   At 500 volts beam damage is recognizable toward the center of the image. Higher magnification imaging can only be achieved using a lower landing voltage.
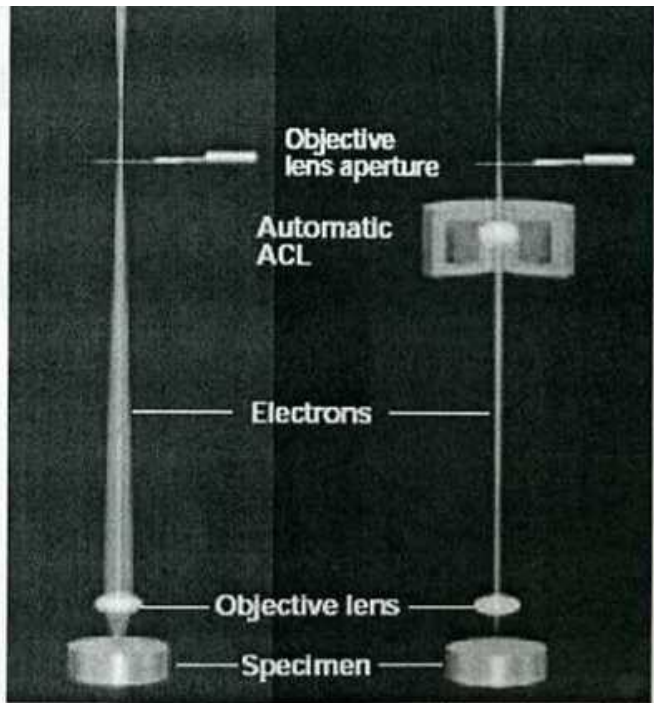

S-4800 0 5kV-D 1 5mm x20 0k SE(U)   2 00um   S-4800 0 1kV-D 1 5mm x20 0k SF(U)   2 00um

500 volts   100 volts

Uncoated, beam sensitive

at small probe sizes

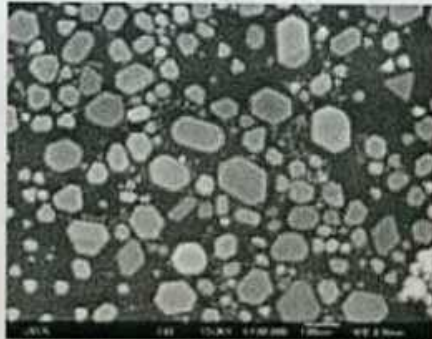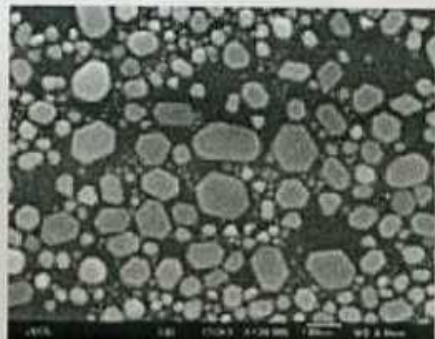Objective lens aperture

Automatic ACL

Electrons

Objective lens

Specimen

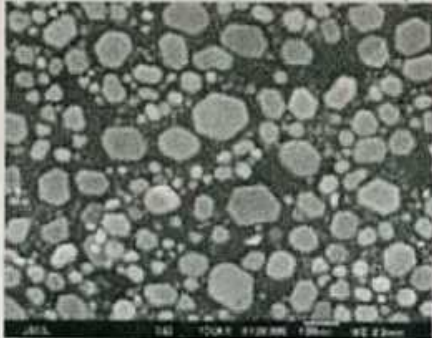Probe diameter is broad at a large probe current condition without the aperture angle control lens (figure left).
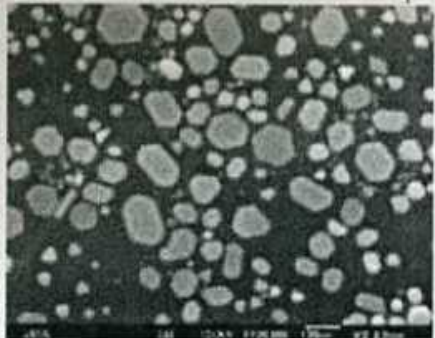
50pA

500pA

Evaporated gold particles   1nA

2nA

DOPANT IMAGING – Sensitive to energy levels

DOPANT IMAGING – Sensitive to energy levels

Schematic diagram of the TLD with trajectories of SEs at large deflector voltage e.g. $D=60V$ (red) and small deflector voltage e.g. $D=9V$ (blue).

n-type Si with 5 phosphorus doped layers as indicated in schematic drawing (a), (b) standard SE image, (c) energy filtered SE image. Note the enhanced contrast in (c).